IEEE Access
Multidisciplinary | Rapid Review | Open Access Journal

Received August 25, 2020, accepted September 19, 2020, date of publication September 28, 2020, date of current version October 8, 2020.

Digital Object Identifier 10.1109/ACCESS.2020.3027313

An Iterative Method With Enhanced Laplacian-Scaled Thresholding for Noise-Robust Compressive Sensing Magnetic Resonance Image Reconstruction

ZHONG-HUA XIE[1], LING-JUN LIU[1], XIAO-YE WANG[1], AND CUI YANG[2]
[1]School of Computer Science and Engineering, Huizhou University, Huizhou 516007, China
[2]School of Electronic and Information Engineering, South China University of Technology, Guangzhou 510641, China

Corresponding author: Ling-Jun Liu (hzuliu@163.com)

This work was supported in part by the National Natural Science Foundation of China under Grant 62001184, in part by the Guangdong Basic and Applied Basic Research Foundation under Grant 2019A1515111087, in part by the Science and Technology Planning Project of Huizhou under Grant 2020SD0403031, in part by the Project of Young Innovative Talents from Educational Commission of Guangdong Province, China, under Grant 2018KQNCX247, in part by the Doctoral Scientific Research Foundation of Huizhou University under Grant 2018JB024 and Grant 2018JB025, in part by the Natural Science Foundation of Guangdong Province under Grant 2020A1515010962, and in part by the Science and Technology Planning Project of Guangzhou under Grant 202002030251.

ABSTRACT Compressive sensing (CS) has proven to be an efficient technique for accelerating magnetic resonance imaging (MRI) acquisition through breaking the Nyquist sampling limit. However, CS measurements are often corrupted by noise in the sensing process, which greatly reduces the quality of reconstructed images and deteriorates the performance of follow-up diagnosis tasks. In this paper, we propose a novel iterative shrinkage-thresholding (IST) method based on enhanced Laplacian-scaled shrinkage operation for robust CS-MRI reconstruction. Differing to existing nonlocal Laplacian-scaled based methods that easily cause biased estimation in the presence of external noise, we design a side information-aided Laplacian-scaled sparse representation model to adapt to spatially varying image structures. Reference information obtained by performing Block-Matching 3D (BM3D) thresholding on the noisy observation is incorporated into the Laplacian-scaled thresholding operator for enhancing the accuracy of sparse coding. Furthermore, we build connections between IST algorithm and approximate message passing (AMP) algorithm and consider an approximation of the divergence of thresholding, leading to an AMP-like iterative method. Experiments validate the effectiveness of leveraging a combination of Laplacian-scaled and BM3D thresholding, and demonstrate the superior robustness of the proposed method both quantitatively and visually as compared with state-of-the-art methods.

INDEX TERMS Compressive sensing (CS), magnetic resonance imaging (MRI), Laplacian-scaled thresholding, BM3D, iterative shrinkage-thresholding (IST), approximate message passing (AMP).

I. INTRODUCTION

Magnetic resonance imaging (MRI) [1] which is a noninvasive, nonionizing imaging modality and offers a variety of contrast mechanisms and excellent visualization of anatomical structure, has been widely used in routine clinical practice. Much research on MRI has focused on the reduction of the acquisition time and accurate reconstruction from highly undersampled k-space data, which is a pair of contradictions. Compressive sensing (CS) methods [2], [3] as a fundamental developed methodology in information society are able to achieve accurate image reconstruction from very few linear measurements, and have been successfully applied to MRI, which is known as CS-MRI [4], [5]. Using CS-MRI techniques one can significantly reduce the amount of k-space data and corresponding acquisition time by means of undersampling without having to sacrifice the quality of reconstructed MR images.

The associate editor coordinating the review of this manuscript and approving it for publication was Hengyong Yu.

The main challenge for CS-MRI reconstruction methods is to find an algorithm that takes into account the undersampling undergone and can compensate the missing data with the prior knowledge of MR images. CS-MRI reconstruction algorithms include greedy algorithms such as matching pursuit (MP) and orthogonal matching pursuit (OMP) [6], iterative optimization algorithms and their variations such as fast iterative shrinkage–thresholding algorithm (FISTA) [7], a shorthand for Nesterov's algorithm (NESTA) [8], alternating direction method of multipliers (ADMM) [9], Bregman iterative algorithms [10], and Bayesian methods such as sparse Bayesian learning (SBL) algorithms [11] and approximate message passing (AMP) and its variations [12], [13].

Greedy algorithms aim to pursuit the sparsest solution of underdetermined CS system while enforce adherence to the observation through least squares fitting [6]. Iterative optimization algorithms often contain the optimization of the data fitting term and the regularization term where shrinkage-thresholding operators are commonly used. In [8], for achieving fast convergence rate and low computational cost, two algorithms with convex relaxation that are based on FISTA and NESTA frameworks respectively have been designed to solve the tree-based MRI problem. With regard to more complicated optimization functions, such as low rank approximation and structural total variation (TV) regularization, ADMM and Bregman iterative algorithms are frequently used to make the optimization more easily be solved. In [9], the low rank inverse problem is extended to an augmented Lagrangian that is solved by ADMM. Bayesian methods usually build probabilistic models with statistical distribution of signals, taking the distribution of both the observation model and the prior into account. Markov Chain Monte Carlo (MCMC) and variational Bayesian (VB) [14] are often employed to implement probabilistic inference in Bayesian methods, which are generally slow. A more efficient Bayesian method AMP with simplified belief propagation is used to do statistical learning in [13]. Among these methods, iterative optimization algorithms such as FISTA, ADMM, and AMP based methods have shown much beneficial to CS-MRI image reconstruction due to their promising performance and efficiency.

CS-MRI reconstruction algorithms share a common characteristic that the regularization term which refers to the prior of images plays an important role. Published works have designed a large number of elaborate prior models, ranging from the well-known total variation (TV) regularization [7], the sparsity-based regularizations with transforms (e.g., DCT and wavelets) [15], the patch-based sparse representation models [16] to structural sparsity-based models [17], [18]. It is assumed that MR images are sparse under analytical transforms in CS-MRI reconstruction methods based on TV model or wavelets [15]. This type of sparsity can be summarized as global sparsity implying that the entire MR image is transformed to a certain sparse domain. However, the global sparsity utilized by these methods is unable to express more complex local edges and textures. By contrast, patch-based sparse representation methods are more effective in representing local image structures with a few elemental structures from a redundant dictionary. With classical dictionary learning (DL) method, DL-MRI [16] learned a small patch-based synthesis while simultaneously performing image reconstruction, however, it ignores the relationship among patches, and has a computationally expensive dictionary learning step.

More sophisticated models i.e., structural sparsity-based models have been incorporated into the reconstruction framework, including tree-structured wavelet sparsity [13], [17], and nonlocal sparsity which refers to the self-similarity in MR images [18], [19]. Hidden Markov tree (HMT) statistical model has been established in the Bayesian reconstruction method Turbo-AMP [13], while iterative optimization algorithms always prefer formulating regularization terms of wavelet tree [12]. Tree-structured wavelet sparsity can be classified into the category of global sparsity essentially, thus also has the intrinsic deficiency of global sparsity-based methods, i.e., lacking adaptability to local image patterns. By contrast, nonlocal similarity belongs to patch-based structural sparsity which describes the resemblance of small image patches in an image, and is often depicted by regularization terms, filtering-based models and composite sparse models. Regularization terms can categorized as follows: the nonlocal total variation (NLTV) regularization [20] which exploits the nonlocal sparsity in gradient domain, patch-based nonlocal operator (PANO) [21] that uses semi-adaptive wavelets, nonlocal low-rank regularization [22] that characterizes the low-rank property of the two-dimensional data matrix grouped by similar patches of MR image. Filtering-based models or called plug-and-play priors are usually related to the Block-Matching 3D (BM3D) filtering method [23], where similar 2D image blocks are grouped into 3D data arrays and then collaborative filtering is used for denoising. D-AMP [24], BM3D-IT [25] and BM3D-AMP-MRI [26] belong to this kind of algorithm. Composite sparse models developed to soften and complement the nonlocal sparsity have been shown to provide enhanced performance, including a combination of low-rank regularization and TV regularization [27], a low-rank plus learned dictionary-sparse model [28] and a composite sparse model that combines low-rank modeling and block matching with transform learning for capturing both local and global features [29]. Recently, deep neural networks have achieved exciting success for accelerating MRI. Reconstruction algorithms of this class can be divided into two subcategories. In the first category, deep neural networks are employed to learn mapping functions from measurements or zero-filled image to high-resolution MR image, such as AutoMap [30] and CS with Generative Adversarial Networks (GANCS) [31]. In the second category, iterative algorithms are explicitly unrolled and turned into neural nets, such as ADMM-Net [32], ISTA-Net [33] and Learned-DAMP [34]. However, these methods are held back by the fact that the theory governing their performance needs to be strengthened, and has to pre-train with a lot of time and vast amounts of data, but large datasets of MRI are rare.

Despite the great progress, the performance of CS-MRI reconstruction method may degrade severely in the presence of external noise, especially for deep learning-based methods. In this work, we propose a novel iterative shrinkage-thresholding method based on side information-aided Laplacian-scaled sparse representation model for robust CS-MRI reconstruction. We use Laplacian scale mixture (LSM) [35], [36] model to represent the sparse coefficients packed by similar patches of the MR image, and turn the simultaneous sparse coding procedure into a thresholding operator called Laplacian-scaled thresholding operator. Reference information obtained by BM3D thresholding at each iteration is provided to help Laplacian-scaled thresholding distinguish between noise and image components and reduce the biased estimation problem, therefore, side information-aided Laplacian-scaled thresholding model can be regarded as an ingenious combination of Laplacian-scaled thresholding and BM3D thresholding. Furthermore, our iterative method is an AMP-like method, implying that our method has the Onsager correction term, however, the divergences of thresholding is approximated to predetermined constants. We have observed that using predetermined constants does not degrade the reconstruction performance but reduces the computational complexity when the partial Fourier measurement matrix is used. It is shown in experiments that our method is more robust to noise when compared to state-of-the-art methods.

II. BACKGROUND

A. COMPRESSIVE SENSING MAGNETIC RESONANCE IMAGING

Applying CS theory in magnetic resonance imaging (MRI), the MR scanning time can be significantly reduced. The observation or data acquisition forward model for MR image reconstruction can eventually be approximated as a discretized linear system:

$$y = Ax + w \tag{1}$$

where $x \in \mathbb{C}^n$ is the vectorization result of a MR image, $A \in \mathbb{C}^{m\times n}$ is a partial Fourier transform, $y \in \mathbb{C}^m$ is the sampling measurement of x i.e., the undersampled k-space data, and w denotes the additive noise. Since $m < n$, the inverse problem of CS is underdetermined. Fortunately, MR images are generally sparse and thus are able to reconstructed based on CS theory. The MRI is first modeled as a CS problem in SparseMRI [37]:

$$x = \arg\min_x \frac{1}{2}\|y - Ax\|_2^2 + \rho\|x\|_{\mathrm{TV}} + \lambda\|\Psi x\|_1 \tag{2}$$

In (2), Ψ denotes the wavelet transform, ρ and λ are two regularization parameters. The sparsity regularization is the linear combination of total variation and wavelet sparsity regularization, which is based on the observation that the piecewise smooth MR images of organs can be sparsely represented by the wavelet basis and should have small total variations. To solve this model, the non-smooth l_1 norm term is transformed a smooth one by introducing an approximated problem, which is then solved by the classical conjugate gradient (CG) method [37]. The disadvantage of this method is that no structural prior information is utilized other than sparsity.

B. STRUCTURAL SPARSITY-BASED CS-MRI

Owing to the fact that the wavelet coefficients of real MR images tend to be quadtree structured, wavelet tree sparsity MRI (WaTMRI) [17] improves the reconstruction model in (2) by introducing one more regularization term with tree sparsity

$$x = \arg\min_x \frac{1}{2}\|y-Ax\|_2^2+\rho\|x\|_{\mathrm{TV}}+\lambda(\|\Psi x\|_1+\sum_{x_i\in Q}\|\Psi x_i\|_2) \tag{3}$$

where Q denotes the set of all parent-child groups for the wavelet quadtree and x_i is one of such groups. Based on the FISTA algorithm, this problem is solved very efficiently Although it has improved the reconstruction result, it is still a global sparsity-based method, which has the deficiency of lacking adaptability to various local patterns.

The nonlocal sparsity referred to the fact that MR images have abundant self-repeating patterns has shown more beneficial to CS-MRI image reconstruction due to its better spatial adaptation. In the work of CS recovery via nonlocal low-rank regularization (NLR-CS) [22], a nonlocal sparsity-based model that reflects the group sparsity of similar patches with a low-rank regularization term for CS recovery is established and can be formulated as follows

$$x = \arg\min_x \frac{1}{2}\|y-Ax\|_2^2+\rho\sum_{i=1}^{G}\{\|X_i-L_i\|_F^2+\lambda\|L_i\|_*\} \tag{4}$$

where $X_i \in \mathbb{R}^{M\times N}$ is a 2D matrix formed by similar patches, G is the total number of similar patch groups, L_i is the low-rank data matrices to be estimated, $\|L_i\|_*$ is the nuclear norm of L_i, taking a sum value of its singular values, i.e., $\|L_i\|_* = \sum_j |l_{i,j}|$ where $l_i = [l_{i,1}, l_{i,2}, \ldots, l_{i,N}]$ denotes the singular value vector of L_i. This objective functional is solved by alternatively minimizing the objective functional with respect to the whole image x and low-rank data matrices L_i.

C. ITERATIVE ALGORITHMS

We can solve the above minimizing problems efficiently with alternate optimization algorithms such as iterative shrinkage-thresholding (IST) method [38] and approximate message passing (AMP) algorithm [12]. As an example, we consider solving $\min_x \|y - Ax\|_2^2/2 + \lambda\|\Psi x\|_1$. The alternating expressions in the IST algorithm are

$$x^{(t+1)} = \eta(x^{(t)} + A^* z^{(t)}) \tag{5}$$

$$z^{(t)} = y - Ax^{(t)} \tag{6}$$

while the ones in the AMP algorithm are

$$x^{(t+1)} = \eta(x^{(t)} + A^* z^{(t)}) \tag{7}$$

$$z^{(t)} = y - Ax^{(t)} + \frac{z^{(t-1)}}{m} \left\| \eta'(x^{(t-1)} + A^* z^{(t-1)}) \right\|_1 \tag{8}$$

where $x^{(t)}$ and $z^{(t)}$ are the estimates of x and the residual at iteration t. The iteration starts from $x^{(0)} = 0$, $z^{(0)} = y$. A^* is the conjugate transpose of A. The functions $\eta(\cdot)$ and $\eta'(\cdot)$ are the wavelet threshold function and its first derivative respectively. These two algorithms are very similar except for the last term in Eq. (8) called the Onsager correction term which is introduced by AMP to approximately Gaussianize the residual error at each iteration and thus makes existing Gaussian denoisers more effective when compared to other iterative solvers. Some AMP variants have been proposed with various forms of regularizers, such as total variation, a Cauchy prior in the wavelet domain [39] and a plug-and-play prior which employs BM3D denoiser as an image prior [24].

III. A NOVEL ITERATIVE METHOD WITH LAPLACIAN-SCALED THRESHOLDING AND BM3D THRESHOLDING

A. AN AMP-LIKE ITERATIVE METHOD

We consider the connection between the IST method and the AMP method, which enables us to greatly improve the performance of the conventional IST, and leads to a novel iterative method for robust MR image reconstruction. To this end, we transform the AMP method into a special IST method by introducing three auxiliary variables $q^{(t)} = x^{(t)} + A^* z^{(t)}$, $d^{(t)} = \left\| \eta'(x^{(t-1)} + A^* z^{(t-1)}) \right\|_1 / m$ where $d^{(0)} = 1$, $f(x) = \|y - Ax\|_2^2/2$ and then replace the $z^{(t)}$ in $q^{(t)} = x^{(t)} + A^* z^{(t)}$ with Eq. (8)

$$\begin{aligned} q^{(t)} &= x^{(t)} + A^*(y - Ax^{(t)} + z^{(t-1)} d^{(t-1)}) \\ &= x^{(t)} - \nabla f(x^{(t)}) + A^* z^{(t-1)} d^{(t-1)} \\ &= x^{(t)} - \sum_{i=1}^{t} \nabla f(x^{(i)}) d^{(0)} d^{(1)} \dots d^{(t-i)} \end{aligned} \tag{9}$$

where $\nabla f(x^{(t)})$ represents the gradient of $f(x)$ at point $x^{(t)}$. Therefore, the AMP method can be rewritten as $x^{(t+1)} = \eta(q^{(t)})$ where $q^{(t)}$ computed by Eq. (9) can be regarded as a temporary noisy image. The compution of $q^{(t)}$ is expressed as

$$q^{(t)} = x^{(t)} - \nabla f(x^{(t)}) \tag{10}$$

It is shown in Eq. (9) and Eq. (10) that the AMP method uses a linear combination of gradients of the preceding iteration solutions while the conventional IST method takes only the gradient of the current iteration solution. When the AMP algorithm is combined with the structural sparsity, the shrinkage operator $\ell(\cdot)$ will become non derivable for the result that they do not have an explicit input-output relation. Fortunately, the Monte Carlo (MC) method has been applied to simulate the derivative with random numbers in the work of D-AMP [24], but it is time-consumed. In order to reduce running time, we use predetermined constants to approximate the derivative which is pre-trained with data based on the observation that the evolutions of derivative along with iteration for different images perform similar under the same specific experimental settings, including sampling ratio and the strength of external noise. Furthermore, motivated by the effective acceleration scheme in fast iterative shrinkage-thresholding algorithm (FISTA) [7], the simplified AMP method is further accelerated with additional acceleration steps i.e. Eq. (13) and Eq. (14). Our proposed method has the following alternating expressions

$$q^{(t)} = x^{(t)} - \sum_{i=1}^{t} \nabla f(x^{(i)}) c^{(0)} c^{(1)} \dots c^{(t-i)} \tag{11}$$

$$x^{(t+1)} = \ell(q^{(t)}) \tag{12}$$

$$u^{(t+1)} = (1 + \sqrt{1 + 4(u^{(t)})^2}) \Big/ 2 \tag{13}$$

$$x^{(t+1)} = x^{(t+1)} + \left(\frac{u^{(t)} - 1}{u^{(t+1)}}\right)(x^{(t+1)} - x^{(t)}) \tag{14}$$

where $c^{(0)}, c^{(1)}, \dots, c^{(t-1)}$ are predetermined constants, $u^{(1)} = 1$, $x^{(0)} = 0$. $\ell(\cdot)$ in Eq. (12) is a shrinkage operator associated with the nonlocal sparse reconstruction through the combination of Laplacian-scaled and BM3D thresholding which can be viewed as the engine of our method.

B. EXPLORING THE POWER OF COMPLEMENTARY REGULARIZERS

Although a number of complementary regularizers [27]–[29] have been proposed to improve the performance of CS-MRI reconstruction, most of these method combines a nonlocal regularizer with a local (or global) regularizer e.g. low-rank regularization plus learned dictionary-sparse model [28] (or TV regularization [27]) for the purpose of fully utilizing both the nonlocal and local (or global) image properties. In this work, we propose employing two nonlocal regularizers to explore the power of complementary regularizers. Laplacian-scaled thresholding operator which will be elaborated later is based on the nonlocal mean method (a denoising algorithm in spatial domain), while the BM3D method is a well-known image denoising algorithm in frequency domain. Combining both methods brings us a dual domain method and ensures a more accurate parameter estimation in Laplacian-scaled thresholding especially in the noisy environment.

The plug-and-play prior framework [40], [41] offers simple integration between inversion problems and priors, and allows that the prior to be used does not have to be explicitly formulated as a penalty expression. We consider the following composite sparse problem for CS-MRI

$$x = \arg\min_x \frac{1}{2} \|y - Ax\|_2^2 + \lambda g(x) + \rho h(x) \tag{15}$$

Generally, $g(x)$ and $h(x)$ can be arbitrary regularizers. Applying our proposed iterative method to solve this composite sparse problem will only lead to a change in the

formula (12), which becomes solving the following proximal problem

$$x = \arg\min_x \frac{1}{2}\|x-q\|_2^2 + \lambda g(x) + \rho h(x) \tag{16}$$

This composite problem can easily be solved by the method of composite splitting algorithm (CSA) [42]. CSA decomposes the difficult composite regularization problem (16) into two simpler regularization subproblems, and solves each of them very efficiently. Then we have the following subproblems

$$x_1 = \arg\min_x \frac{1}{2}\|x-q\|_2^2 + \frac{\lambda}{\omega_1} g(x) \tag{17}$$

$$x_2 = \arg\min_x \frac{1}{2}\|x-q\|_2^2 + \frac{\rho}{\omega_2} h(x) \tag{18}$$

The solutions of Eq. (17) and Eq. (18) x_1 and x_2 corresponds to the denoised results of Laplacian-scaled thresholding and BM3D thresholding respectively. Finally, the solution of Eq. (16) is obtained by linear combination of x_1 and x_2 with the weights ω_1 and ω_2 as follows

$$x = \omega_1 x_1 + \omega_2 x_2 \tag{19}$$

The conclusion that the solution of the composite sparse problem is the average of the results obtained by the two thresholding operations seems quite reasonable, which enables us to achieve an easy and flexible combination of arbitrary regularizers.

The BM3D thresholding is derived from the BM3D method [23]. In the original version of BM3D, there is a secondary Wiener filtering step, however, we found that using the full denoising setup with the Wiener filter does not significantly enhance the reconstruction performance despite the increased computational complexity. Thus, we only consider the initial hard thresholding step of the BM3D method which is offered as follows

$$h(x) = \sum\nolimits_{i=1}^{G} \left\| \Phi \tilde{X}_i \right\|_0 \tag{20}$$

where Φ denotes the 3D wavelet transform and $\tilde{X}_i$ denotes the i-th 3D group.

C. SIDE INFORMATION-AIDED LAPLACIAN-SCALED THRESHOLDING

As for Laplacian-scaled thresholding i.e. solving Eq. (17), we model sparse coefficients related to similar patches of MR image with Laplacian scale mixture (LSM) distribution, and regard the solving process of the sparse coding problem as a thresholding operator. LSM distribution has been widely utilized in modeling sparse coefficients of signal, such as the sparse coefficients of local patches of natural images in [35], the tensor coefficients of multi-frame images in [36], and the sparse impulse noise in [43]. In our previous work [5], we have applied LSM model in describing the nonlocal sparsity of MR images. We extend the previous model to a side information-aided Laplacian-scaled model which can exploit the reference information provided by the BM3D thresholding to enhance the robustness of our method.

In order to design our Laplacian-scaled thresholding operator, we consider the denoising problem $y = x + v$, where $v \sim N(0, \sigma^2)$ denotes the additive Gaussian noise. We define the Laplacian scale mixture distribution as

$$p(\alpha_i) = \int_0^\infty p(\alpha_i|\theta_i)p(\theta_i)d\theta_i \tag{21}$$

where $\alpha_i = \theta_i\beta_i$ represents the sparse coefficient. The multiplier variable θ_i is a positive random variable with probability $p(\theta_i)$, and β_i has a Laplacian distribution with scale 1. Supposing that β_i and θ_i are independent, conditioned on the parameter θ_i, the coefficient α_i has a Laplacian distribution $p(\alpha_i|\theta_i) = \theta_i^{-1}\exp(-\theta_i^{-1}|\alpha_i|)\big/2$. The side information-aided sparse coding model of x_i can be interpreted as a Maximum a Posterior (MAP) estimation

$$\begin{aligned}(\alpha_i, \theta_i) &= \arg\min_{\alpha_i,\theta_i} p(\alpha_i, \theta_i|x_i, s_i) \\ &= \arg\min_{\alpha_i,\theta_i} p(x_i, s_i|\alpha_i, \theta_i)p(\alpha_i, \theta_i) \\ &= \arg\min_{\alpha_i,\theta_i} p(x_i|\alpha_i, \theta_i)p(s_i|\alpha_i, \theta_i)p(\alpha_i|\theta_i)p(\theta_i)\end{aligned} \tag{22}$$

where s denotes the side information which is supposed to be independent with x. First, we have the following likelihood through the assumption that v is white Gaussian noise with variance σ^2. Thus,

$$p(x|\alpha, \theta) = \frac{1}{\sqrt{2\pi\sigma^2}}\exp(-\frac{1}{2\sigma^2}\|x - D\alpha\|_2^2) \tag{23}$$

Second, the prior term can be expressed as

$$p(\alpha|\theta) = \prod_i p(\alpha_i|\theta_i) = \prod_i \frac{1}{2\theta_i}\exp(-\frac{|\alpha_i - \mu_i|}{\theta_i}) \tag{24}$$

Third, the noninformative prior is adopted for the scale parameter θ

$$p(\theta) = \prod_i p(\theta_i) = \prod_i \frac{1}{\theta_i} \tag{25}$$

At last, we might propose the distribution of the side information to be subject to Gaussian distribution

$$p(s|\alpha, \theta) = \frac{1}{\sqrt{2\pi\sigma_s^2}}\exp(-\frac{1}{2\sigma_s^2}\|s - D\alpha\|_2^2) \tag{26}$$

It is reasonable that the sparse representation $D\alpha$ should be close to the denoised result i.e. s produced by the BM3D thresholding. Note that, the initial estimation of x in Eq. (23) is the noisy input obtained via Eq. (11). It is helpful to implement sparse decomposition using a denoised result which can be regarded as side information besides using the noisy input itself especially when the CS measurements are seriously polluted by noise. Finally, we can translate the MAP estimation problem in log domain into the following optimization problem

$$\begin{aligned}(\alpha, \theta, \mu) = \arg\min_{\alpha,\theta,\mu} &\frac{\|x - Da\|_2^2}{2\sigma^2} + \frac{\|s - Da\|_2^2}{2\sigma_s^2} \\ &+ \sum_i \frac{|\alpha_i - \mu_i|}{\theta_i} + 2\sum_i \log\theta_i\end{aligned} \tag{27}$$

This objective function is similar to the one in our previous work [5], except for the second term which introduces an extra reference for the data fitting. We further simplify the objective function by translating it from (α, θ, μ) domain to (β, θ, τ) domain

$$(\beta, \theta, \tau) = \arg\min_{\beta,\theta,\tau} \frac{\|x - D\Lambda\beta\|_2^2}{2\sigma^2} + \frac{\|s - D\Lambda\beta\|_2^2}{2\sigma_s^2} + \|\beta - \tau\|_1 + 2\log\theta \quad (28)$$

where $\Lambda = \mathrm{diag}(\theta_i)$ is a diagonal matrix. Note that $\alpha = \Lambda\beta$ and $\mu = \Lambda\tau$. For a collection of similar patches, their corresponding sparse coefficients should be characterized by the same prior, thus, this sparse coding problem is then extended to a structured sparse coding problem

$$(B, \theta, \Pi) = \arg\min_{B,\theta,\Pi} \frac{\|X - D\Lambda B\|_F^2}{2\sigma^2} + \frac{\|S - D\Lambda B\|_2^2}{2\sigma_s^2} + \|B - \Pi\|_1 + 2\log(\theta + \varepsilon) \quad (29)$$

where $B = [\beta_1, \beta_2, \ldots, \beta_k] \in \mathbb{R}^{k\times k}$, $\Pi = [\tau_1, \tau_2, \ldots, \tau_k] \in \mathbb{R}^{k\times k}$. ε is a small positive number introduced for numerical stability, because $\log\theta$ is unstable as $\theta \to 0$.

To solve this problem, we can resort to the method of alternating optimization. First, we compute Π for a fixed (B, θ). Given a collection of similar patches, the nonlocal mean filter is adopted to estimate the location parameter of LSM model μ

$$\mu = \sum\nolimits_j \omega_j \alpha_j \quad (30)$$

where the weight $\omega_j = \exp(-\|h - h_j\|_2^2 / \delta)$. Once we have the location parameter μ, τ related to Π is computed by

$$\tau = \Lambda^{-1}\mu \quad (31)$$

To obtain the initial estimation of sparse coefficient $\alpha^{(0)}$ and scale parameter θ^0, we compute the principal component analysis (PCA) basis D_i for each similar image patches X_i which is set equal to the noisy input in the beginning i.e., $x = q + (\sigma^2/\sigma_s^2)s$, and then have the initial estimation of sparse coefficients by $\alpha^{(0)} = D_i^{-1}X_i$. The initial estimation of scale parameter is computed with one-sample maximum-likelihood (ML) estimation

$$\theta^0 = \sqrt{\max((\alpha_i^0)^2 / k - \sigma^2, 0)} \quad (32)$$

Second, for a fixed (B, Π), one can update θ by solving

$$\theta = \arg\min_{\theta} \frac{\|X - D\Lambda B\|_F^2}{2\sigma^2} + \frac{\|S - D\Lambda B\|_2^2}{2\sigma_s^2} + 2\log(\theta + \varepsilon) \quad (33)$$

Since the dictionary D is orthogonal, this can be rewritten as

$$\theta = \arg\min_{\theta} \left\| \frac{\hat{X} + (\sigma^2/\sigma_s^2)\hat{S}}{1 + (\sigma^2/\sigma_s^2)} - \Lambda B \right\|_F^2 + 4\sigma^2\log(\theta + \varepsilon) \quad (34)$$

where $X = D\hat{X}$ and $S = D\hat{S}$. The above minimization problem can be further reduced to a set of scalar minimization problems, one of which denoted by $l(\theta_i)$ is

$$\theta_i = \arg\min_{\theta_i} a_i\theta_i^2 + b_i\theta_i + c\log(\theta_i + \varepsilon) \quad (35)$$

where $a_i = \|\phi_i\|_2^2$, $b_i = -2\phi_i(\varphi_i)^{\mathrm{T}}$ and $c = 4\sigma^2$. ϕ_i and φ_i are the i-th row of B and $C = (1 + (\sigma^2/\sigma_s^2))^{-1}(\hat{X} + (\sigma^2/\sigma_s^2)\hat{S})$ respectively. The superscript T denotes the transposition operation. The solution to this quadratic equation is

$$\theta_i = \begin{cases} 0, & \text{if } b_i^2/(16a_i^2) - c/(2a_i) < 0 \\ \min\{l(0), l(\theta_{i,1}), l(\theta_{i,2})\}, & \\ \quad \text{otherwise} & \end{cases} \quad (36)$$

where $\theta_{i,1} = -\frac{b_i}{4a_i} + \sqrt{\frac{b_i^2}{16} - \frac{c}{2a_i}}$, $\theta_{i,2} = -\frac{b_i}{4a_i} - \sqrt{\frac{b_i^2}{16} - \frac{c}{2a_i}}$. The discussions of this result are similar to the ones in our previous work (please refer to ref. [5]), however, C is changed which is caused by introducing reference information. At last, we compute B for a fixed (θ, Π). The subproblem simply becomes

$$B = \arg\min_{B} \|X - D\Lambda B\|_F^2 + \left\|(\sigma^2/\sigma_s^2)(S - D\Lambda B)\right\|_2^2 + 2\sigma^2\|B - \Pi\|_1 \quad (37)$$

This problem has a closed-form solution via soft thresholding

$$B_i = \frac{\mathrm{diag}(\theta_{i,j}^{-1})}{1 + (\sigma^2/\sigma_s^2)}(\Omega_{\gamma_i}(D_i^{\mathrm{T}}X_i + (\sigma^2/\sigma_s^2)D_i^{\mathrm{T}}S_i - \mu_i) + \mu_i) \quad (38)$$

where $\Omega(\cdot)$ denotes the soft-thresholding operator with a threshold $\gamma_i = (2\sigma^2)/\theta_i^2$. The variance of noise σ^2 can be obtained by maximum likelihood estimation

$$(\sigma^{(t)})^2 = \left\|q^{(t)} - x^{(t)}\right\|_2^2 / m \quad (39)$$

Finally, we have our side information-aided Laplacian-scaled thresholding operator i.e. Eq. (38). The final output of the structured sparse coding for a given similar patches group is $D_i\Lambda_i B_i$. Then the denoised MR image can be recovered by averaging all reconstructed patches at the same location.

It is unnecessary to determine the specific values of two regularization parameters ρ and λ in Eq. (15), which are intrinsically connected with the thresholds of denoising, and have been integrated into the thresholds of our BM3D and Laplacian-scaled thresholding operators. The thresholds are $0.8\sigma^2$ and $2.5 \times (2\sigma^2)/\theta_i^2$ respectively in our experimental setting. Furthermore, the constants $c^{(0)}, c^{(1)}, \ldots, c^{(t-1)}$ can be set according to the values simulated by the method of Monte Carlo (MC) [24] through a pre-training procedure. In our simulations, the constants $c^{(0)}, c^{(1)}, \ldots, c^{(t-1)}$ are equal to the value at the stable stage of iterations obtained by MC with pre-training. At last, we want to determine the value of σ_s^2 in the side information-aided term. According to Eq. (27), a smaller value of σ_s^2 means a greater weight of the

item of side information. We have observed that a wide range of values can help improve the reconstruction performance in the presence of external noise, while the item of side information has little usefulness when there is no external noise. For the sake of simplicity, we set $\sigma_s^2 = (5/3)\sigma^2$ when using noisy measurements, and remove the side information-aided term when using noiseless measurements. In general, the proposed algorithm is summarized in **Algorithm 1** named as CS via enhanced Laplacian-scaled thresholding (ELT-CS). Exploring the power of complementary regularizers and assisting with side information as two kinds of enhanced strategy have been implemented in our method for robust MR image reconstruction.

Algorithm 1 CS via Enhanced Laplacian-Scaled Thresholding

Input: $y, A, T, \omega_1, \omega_2, x^0 = 0, z^0 = y$.
For $t = 1$ **to** T **do**

(1) Obtain the temporary noisy image $q^{(t)}$ with Eq. (11).
(2) Estimate the noise variance $(\sigma^{(t)})^2 = \left\|q^{(t)} - x^{(t)}\right\|_2^2 / m$.
(3) Perform the denoising operator $x^{(t+1)} = \ell(q^{(t)})$ as follows:
  (I) Perform the BM3D thresholding on $q^{(t)}$ to get the reconstructed image $x_1^{(t+1)}$.
  (II) Perform the side information-aided Laplacian-scaled thresholding on $q^{(t)}$ to get the reconstructed image $x_2^{(t+1)}$ as follows:
    (a) Construct the matrix of similar patches with the image $q^{(t)} + (\sigma^2/\sigma_s^2)x_1^{(t+1)}$ and compute the PCA basis D_i.
    (b) Estimate the location parameter of LSM μ and then obtain Π with Eq. (31).
    (c) Estimate the scale parameter of LSM θ with Eq. (36).
    (d) Estimate the sparse coefficient matrix B with Eq. (38).
    (e) Obtain all the denoised matrix $D_i\Lambda_i B_i$ and recover the whole MR image $x_2^{(t+1)}$.
(4) Obtain $x^{(t+1)}$ by linear combination of $x_1^{(t+1)}$ and $x_2^{(t+1)}$ i.e. $x^{(t+1)} = \omega_1 x_1^{(t+1)} + \omega_2 x_2^{(t+1)}$.
(5) Perform the acceleration steps:
$u^{(t+1)} = (1 + \sqrt{1 + 4(u^{(t)})^2})/2$,
$x^{(t+1)} = x^{(t+1)} + (\frac{u^{(t)}-1}{u^{(t+1)}})(x^{(t+1)} - x^{(t)})$.

IV. EXPERIMENTS

In order to verify the excellent robustness of the proposed ELT-CS for MR image reconstruction in the presence of external noise, we compare it with nine CS algorithms, including two deep learning-based algorithms ADMM-Net [32] and TGDOF [44] and seven nonlocal sparsity-based algorithms PANO [21], BM3D-IT [25], BM3D-AMP-MRI [26], NLR-CS [22], D-AMP [24], CS via BM3D thresholding (BM3DT-CS) and CS via Laplacian-scaled thresholding (LT-CS) where BM3DT-CS and LT-CS are derived from our ELT-CS method by only using the BM3D thresholding and the Laplacian-scaled thresholding respectively. Through the comparisons between ELT-CS and BM3D-CS, LT-CS, one can validate the benefit of complementary regularizers and side information. For fair comparisons, we download codes from their websites and adopt the default experiment settings except for NLR-CS. To make NLR-CS more robust to noise, its parameter par.nSig which is set empirically is tuned to par.nSig = par.nSig+σ due to the external noise. As shown in Figure 1, eight standard test MR images with the same size of 256×256 are employed as the experimental images. Both 2D random sampling and pseudo radial sampling schemes are adopted in our algorithms. The sampling masks are shown in Figure 2 and Figure 3 respectively. In the 2D random sampling scheme,

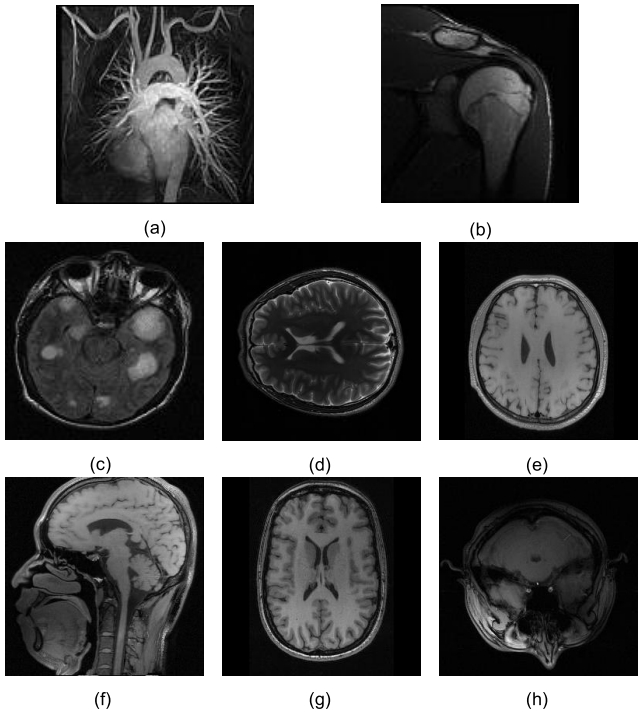

FIGURE 1. Test images used for compressive sensing experiments: (a) Chest; (b) Shoulder; (c) Brain1; (d) Brain2; (e) Brain3; (f) Head; (g) Brain4; (h) Brain5.

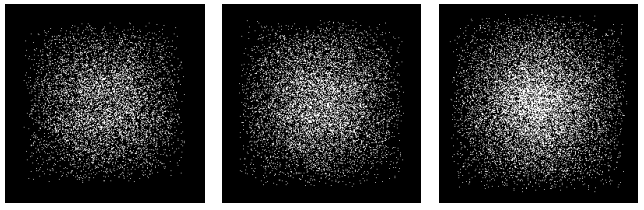

FIGURE 2. 2D random sampling masks used in the experiments: (a) 10% sampling; (b) 12% sampling; (c) 16% sampling.

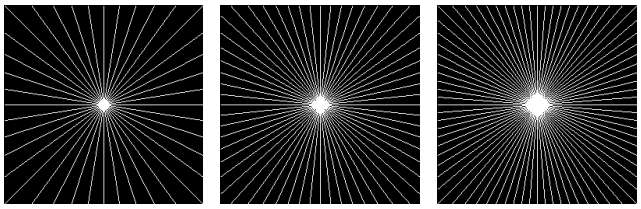

FIGURE 3. Pseudo radial sampling masks used in the experiments: (a) 20 lines; (b) 30 lines; (c) 40 lines.

three sampling rates including 10%, 12% and 16% are chosen for comparisons as we always interesting in low sampling rates because lower sampling ratio needs less MR scanning time to acquire. In the pseudo radial sampling scheme, the numbers of sampling lines directly related to sampling rates on the masks are 20, 30 and 40 respectively. We present the experimental results including objective quality, subjective quality and runtime. The peak signal-to-noise ratio (PSNR), and structural similarity (SSIM) are used to quantitatively evaluate the qualities of the reconstruction results. We generate the CS measurements by randomly sampling the Fourier transform coefficients of test images, and then reconstruct MR images by eight comparison algorithms. For the 2D random sampling scheme, we follow the sampling strategy of previous works [17], [42], which randomly choose more Fourier coefficients from low frequency and less on high frequency. For the pseudo radial sampling scheme, we refer directly to the sampling method in the literature [27].

The main parameters of the proposed ELT-CS algorithm are the weights of the linear combination ω_1 and ω_2 in Eq. (19). $\omega_1 = 0.2$ and $\omega_2 = 0.8$ are chosen empirically when using noiseless measurements, which implies that the method with Laplacian-scaled thresholding is generally better than the one with BM3D. $\omega_1 = 0.1$ and $\omega_2 = 0.9$ or $\omega_1 = -0.2$ and $\omega_2 = 1.2$ can be chosen when using noisy measurements. The reconstructed image produced by BM3D thresholding has been employed as side information in the subsequent Laplacian-scaled thresholding, thus, its weight can be reduced in the step of the linear combination. We have observed that the later set of parameters are a little better in most situations. We follow the method of previous work [22] to construct the matrix of similar patches. 64 most similar patches with size of 8×8 are chosen for each exemplar patch with size, meanwhile, exemplar image patches in every 5 pixels along both horizontal and vertical directions are extracted. We first present the experimental results for noisy CS measurements because we emphasize the strong robustness of ELT-CS and then report the ones using noiseless CS measurements.

A. EXPERIMENTS ON NOISY MEASUREMENTS

Numerous experiments have been conducted to show the superiority of the proposed CS-MRI recovery method ELT-CS in dealing with the issues of noise corruption by comparing with seven existing reconstruction algorithms ADMM-Net [32], TGDOF [44], PANO [21], BM3D-IT [25], BM3D-AMP-MRI [26], NLR-CS [22], D-AMP [24] and two simplified versions of our ELT-CS i.e. BM3DT-CS and LT-CS. We generate noisy CS measurements by adding Gaussian noise with the variance to the under-sampled Fourier transform coefficients of input images. The noise standard deviation (denoted by sigma or σ) is respectively selected as 10, 20, 30 and 40 for both pseudo radial sampling and 2D random sampling scheme. Complete comparisons are present in Table 1, Table 2, Table 3 and Table 4. Table 1 and Table 3 show the PSNR and SSIM results of these methods recovering eight test images under the sampling scheme of pseudo-radial respectively, while Table 2 and Table 4 present the ones with 2D random sampling scheme.

Firstly, we compare ELT-CS with BM3DT-CS and LT-CS. From Table 1, Table 2, Table 3 and Table 4, we can see that ELT-CS always performs better than the other two methods except for very few cases, in which ELT-CS also acquires close results to the second-best method LT-CS. These results demonstrate the benefit of introducing complementary regularizers and side information in enhancing the capability anti-noise. Besides, ELT-CS outperforms than BM3DT-CS in most cases implying that Laplacian-scaled thresholding is generally more suitable for MR image reconstruction than BM3D thresholding due to the better spatial adaptation. The shortcoming of Laplacian-scaled thresholding is that it uses the nonlocal mean method to estimate the location parameter of LSM model which has validated that it has a worse performance than the method of BM3D. Motivated by this, we explore the use of complementary regularizers and side information to achieve an enhance performance.

Secondly, ELT-CS is compared with seven existing reconstruction algorithms. From Table 1, Table 2, Table 3 and Table 4, we can conclude that 1) the quality of the images reconstructed by all CS-MRI methods degrades seriously as the amount of measurement noise increases; 2) the proposed method ELT-CS always achieve the highest PSNR and SSIM values when compared with these seven methods, which has demonstrated the superiority of the proposed method in robustness; 3) two deep learning-based reconstruction methods ADMM-Net and TGDOF do not have the superiority when the CS measurements is contaminated by external noise despite the new trends brought by them due to the fast speed. The average PSNR improvements over ADMM-Net, TGDOF, PANO, BM3D-IT, BM3D-AMP-MRI, NLR-CS, D-AMP are about 3.80 dB, 5.55 dB, 5.36 dB, 1.34 dB, 0.84 dB, 2.91 dB and 0.73 dB when using pseudo-radial sampling, 5.52 dB, 7.21 dB, 4.57 dB, 3.04 dB, 1.43 dB, 3.12 dB and 1.03 dB when using 2D random sampling respectively.

At last, by comparing BM3DT-CS with D-AMP which employs the full steps of the BM3D denoising method and the standard AMP method, we can see the performance of our AMP-like iterative method. As we can see from these tables, BM3DT-CS performs a little worse than D-AMP for most cases caused by the rough approximation of the Onsager

TABLE 1. The PSNR (dB) results of different methods with pseudo radial subsampling scheme with varying amounts of additive white gaussian measurement noise.

Sampling lines	Sigma	Methods	PSNR							
			Chest	Shoulder	Brain1	Brain2	Brain3	Head	Brain4	Brain5
20	10	ADMM-Net	21.39	30.40	25.46	25.72	26.95	23.14	24.74	28.17
		TGDOF	22.57	30.86	28.01	27.90	28.47	24.69	27.32	28.90
		PANO	21.50	29.15	25.18	25.93	26.98	23.08	25.12	27.30
		BM3D-IT	21.18	30.54	25.01	26.49	26.67	22.30	25.41	28.06
		BM3D-AMP-MRI	22.03	32.03	27.07	27.96	28.62	23.66	27.19	29.23
		NLR-CS	21.87	30.74	25.86	25.76	27.56	23.68	26.16	27.56
		D-AMP	22.41	31.90	27.12	27.65	28.63	24.00	27.37	29.22
		BM3DT-CS	22.60	31.93	27.46	27.75	28.77	24.40	27.72	29.15
		LT-CS	22.60	32.84	28.25	28.53	29.53	24.77	28.30	29.51
		ELT-CS	**23.30**	**33.43**	**28.76**	**28.73**	**29.89**	**25.20**	**28.62**	**30.05**
	20	ADMM-Net	20.96	27.72	24.12	24.26	25.00	22.24	23.57	26.20
		TGDOF	21.17	25.88	24.61	24.32	24.71	22.55	24.11	25.03
		PANO	21.01	25.05	23.63	22.94	24.52	22.49	23.46	24.25
		BM3D-IT	21.12	30.27	25.43	26.32	26.86	22.50	25.62	27.66
		BM3D-AMP-MRI	21.92	31.02	26.66	26.91	27.87	23.28	26.26	28.47
		NLR-CS	21.37	29.41	25.51	25.29	26.68	23.20	25.56	26.85
		D-AMP	22.25	31.36	26.45	26.68	27.84	23.55	26.43	28.13
		BM3DT-CS	22.09	30.84	26.73	26.73	27.93	23.55	26.74	28.15
		LT-CS	22.42	31.25	27.46	27.35	28.42	24.21	27.34	28.44
		ELT-CS	**22.86**	**31.73**	**27.74**	**27.65**	**28.81**	**24.42**	**27.59**	**28.80**
	30	ADMM-Net	20.44	26.03	23.04	23.20	23.56	21.44	22.54	24.83
		TGDOF	19.52	22.31	21.67	21.25	21.60	20.38	21.29	21.89
		PANO	20.38	21.88	21.04	20.67	22.38	20.77	21.54	21.40
		BM3D-IT	21.09	29.51	25.25	25.66	26.53	22.52	25.24	27.12
		BM3D-AMP-MRI	21.56	29.84	25.84	25.94	26.96	23.06	25.39	27.69
		NLR-CS	21.12	27.32	24.59	24.17	25.18	22.63	24.33	25.48
		D-AMP	21.98	30.43	25.91	26.04	27.20	23.33	25.78	27.55
		BM3DT-CS	21.88	30.32	25.93	25.92	27.08	23.06	25.66	27.40
		LT-CS	22.10	31.05	26.96	26.42	27.29	23.68	26.36	26.98
		ELT-CS	**22.38**	**31.24**	**27.17**	**26.62**	**27.58**	**23.64**	**26.54**	**28.10**
	40	ADMM-Net	19.94	24.64	22.12	22.21	22.34	20.73	21.66	23.63
		TGDOF	17.88	19.70	19.44	18.86	19.25	18.52	19.06	19.43
		PANO	18.79	19.46	19.08	18.52	20.39	19.72	19.92	19.62
		BM3D-IT	20.91	28.55	24.67	24.99	25.88	22.32	24.47	26.70
		BM3D-AMP-MRI	21.37	28.98	24.94	25.17	26.27	22.51	24.54	26.96
		NLR-CS	20.70	25.40	23.28	22.88	23.67	21.90	23.01	24.02
		D-AMP	21.68	29.89	25.14	25.27	26.58	23.02	25.31	26.77
		BM3DT-CS	21.65	29.77	25.27	25.24	26.50	22.97	25.26	26.70
		LT-CS	21.69	29.89	25.73	25.49	26.73	23.35	25.74	**27.03**
		ELT-CS	**22.16**	**30.41**	**26.34**	**25.83**	**26.85**	**23.43**	**25.93**	26.87
30	10	ADMM-Net	23.45	31.32	27.84	27.64	28.51	25.21	27.52	29.34
		TGDOF	25.00	31.13	28.77	29.01	29.04	26.68	28.19	29.64
		PANO	23.41	29.99	27.48	27.31	28.69	25.07	27.41	28.83
		BM3D-IT	23.17	33.44	27.99	28.88	29.11	24.87	28.43	30.16
		BM3D-AMP-MRI	24.59	34.33	29.61	29.78	30.36	26.32	29.45	30.78
		NLR-CS	24.80	32.96	29.38	28.86	29.65	26.30	29.00	29.89
		D-AMP	24.89	34.23	29.73	29.57	30.29	26.44	29.57	30.62
		BM3DT-CS	24.77	34.21	29.81	29.66	30.30	26.41	29.52	30.72
		LT-CS	24.91	**35.58**	30.45	30.73	**31.57**	27.09	**30.40**	31.56
		ELT-CS	**25.46**	35.53	**30.59**	**30.81**	31.51	**27.24**	30.39	**31.65**
	20	ADMM-Net	22.43	27.84	25.50	25.21	25.86	23.85	25.23	26.72
		TGDOF	22.49	25.17	24.36	24.12	24.27	23.34	23.89	24.61
		PANO	22.55	25.07	24.85	23.52	25.14	23.95	24.45	24.38
		BM3D-IT	23.22	32.19	27.80	27.88	28.61	25.09	27.83	28.81
		BM3D-AMP-MRI	23.99	32.47	28.42	28.25	28.95	25.63	28.08	29.30
		NLR-CS	23.61	29.42	27.36	26.45	27.18	25.06	26.75	27.52
		D-AMP	24.01	32.33	28.38	28.02	29.09	25.54	28.40	29.14
		BM3DT-CS	24.13	32.04	28.43	27.91	28.96	25.59	28.23	29.04
		LT-CS	24.33	33.19	29.15	28.52	29.73	25.87	28.96	29.77
		ELT-CS	**24.85**	**33.25**	**29.28**	**28.86**	**29.84**	**26.13**	**29.18**	**29.91**

TABLE 1. *(Continued.)* **The PSNR (dB) results of different methods with pseudo radial subsampling scheme with varying amounts of additive white gaussian measurement noise.**

30	30	ADMM-Net	21.53	25.75	23.85	23.47	23.98	22.62	23.51	24.81
		TGDOF	19.94	21.44	21.10	20.62	20.73	20.42	20.71	21.12
		PANO	21.62	22.09	22.54	20.57	22.42	21.61	21.91	21.32
		BM3D-IT	22.90	30.86	26.96	27.02	27.77	24.75	26.86	28.08
		BM3D-AMP-MRI	23.39	31.02	27.24	27.15	27.96	24.88	27.07	28.30
		NLR-CS	22.55	26.57	25.30	24.30	24.91	23.67	24.67	25.14
		D-AMP	23.47	31.32	27.38	27.03	28.29	24.89	27.48	28.35
		BM3DT-CS	23.39	31.03	27.22	26.94	28.15	24.76	27.39	28.19
		LT-CS	23.72	31.92	28.02	27.41	28.56	25.12	27.81	28.77
		ELT-CS	**24.00**	**32.02**	**28.10**	**27.61**	**28.74**	**25.27**	**27.97**	**28.84**
	40	ADMM-Net	20.64	24.01	22.51	22.16	22.43	21.45	22.14	23.28
		TGDOF	17.88	18.78	18.82	18.05	18.18	18.33	18.32	18.53
		PANO	19.32	19.66	19.41	18.37	20.19	19.88	19.98	18.89
		BM3D-IT	22.41	29.77	26.10	26.11	26.95	24.02	26.08	27.40
		BM3D-AMP-MRI	22.68	29.81	26.16	26.21	27.11	24.22	26.28	27.45
		NLR-CS	21.46	24.30	23.47	22.51	22.97	22.33	22.85	23.24
		D-AMP	22.86	30.35	26.44	26.13	27.45	24.36	26.63	27.51
		BM3DT-CS	22.82	30.12	26.35	26.07	27.34	24.28	26.54	27.40
		LT-CS	23.08	30.70	26.99	26.41	27.88	24.60	26.96	27.70
		ELT-CS	**23.44**	**30.85**	**27.18**	**26.67**	**27.92**	**24.73**	**27.16**	**27.85**
40	10	ADMM-Net	24.86	31.85	29.24	28.76	29.59	26.61	28.84	30.06
		TGDOF	26.44	30.88	29.22	29.24	29.12	27.27	28.50	29.72
		PANO	25.14	30.66	28.90	28.35	29.51	26.59	28.43	29.71
		BM3D-IT	25.11	35.00	30.42	30.41	30.86	26.97	30.45	31.28
		BM3D-AMP-MRI	26.36	35.48	31.14	30.96	31.65	27.75	30.82	31.90
		NLR-CS	26.38	33.37	30.42	29.63	30.43	27.61	29.80	30.79
		D-AMP	26.84	35.50	31.10	30.69	31.45	27.82	30.57	31.94
		BM3DT-CS	26.88	35.40	31.11	30.74	31.41	27.85	30.56	31.96
		LT-CS	26.82	36.46	31.89	**31.91**	**32.53**	28.67	31.50	**32.57**
		ELT-CS	**27.34**	**36.53**	**31.96**	**31.91**	32.50	**28.74**	**31.56**	32.50
	20	ADMM-Net	23.43	28.00	26.28	25.81	26.34	24.61	25.86	26.86
		TGDOF	22.95	24.85	24.37	23.63	23.75	23.29	23.59	24.35
		PANO	23.80	25.25	25.43	23.72	25.04	24.09	24.81	24.38
		BM3D-IT	25.06	33.18	29.29	28.89	29.76	26.44	29.06	30.11
		BM3D-AMP-MRI	25.49	33.39	29.50	28.96	29.86	26.50	29.15	30.33
		NLR-CS	24.72	29.05	27.68	26.46	27.14	25.66	26.82	27.54
		D-AMP	25.62	33.44	29.53	28.73	29.85	26.62	29.07	30.13
		BM3DT-CS	25.55	33.13	29.39	28.67	29.71	26.54	28.96	29.97
		LT-CS	25.68	**34.15**	30.11	29.58	30.60	27.28	29.83	30.68
		ELT-CS	**26.27**	**34.15**	**30.19**	**29.76**	**30.71**	**27.36**	**29.90**	**30.83**
	30	ADMM-Net	22.13	25.53	24.16	23.71	24.08	22.95	23.71	24.67
		TGDOF	20.00	21.01	20.85	19.93	20.02	20.20	20.22	20.56
		PANO	21.49	21.87	21.49	20.66	22.19	21.84	21.92	21.24
		BM3D-IT	24.36	31.71	28.18	27.63	28.50	25.71	27.89	29.15
		BM3D-AMP-MRI	24.53	31.81	28.27	27.64	28.60	25.74	27.91	29.16
		NLR-CS	23.15	25.85	25.20	23.87	24.42	23.80	24.31	24.77
		D-AMP	24.83	32.14	28.47	27.66	28.84	25.78	28.08	29.09
		BM3DT-CS	24.67	31.59	28.23	27.49	28.64	25.63	27.89	28.81
		LT-CS	24.90	32.62	28.83	28.17	29.28	26.24	28.54	29.60
		ELT-CS	**25.30**	**32.77**	**28.95**	**28.32**	**29.45**	**26.33**	**28.65**	**29.61**
	40	ADMM-Net	20.96	23.59	22.51	22.07	22.27	21.56	22.02	22.89
		TGDOF	17.74	18.22	18.30	17.24	17.30	17.90	17.68	17.74
		PANO	19.70	19.24	19.16	18.44	19.70	19.90	19.78	18.78
		BM3D-IT	23.73	30.48	27.25	26.70	27.59	24.98	26.92	28.18
		BM3D-AMP-MRI	23.78	30.55	27.32	26.74	27.63	25.02	26.98	28.17
		NLR-CS	21.74	23.41	23.09	21.87	22.24	22.15	22.25	22.55
		D-AMP	23.98	31.18	27.50	26.53	27.89	25.11	27.21	28.15
		BM3DT-CS	23.88	30.81	27.34	26.41	27.72	24.94	27.05	27.94
		LT-CS	23.92	31.40	27.83	26.99	28.35	25.35	27.52	28.60
		ELT-CS	**24.55**	**31.57**	**28.01**	**27.10**	**28.40**	**25.47**	**27.67**	**28.74**

correction term. However, BM3DT-CS is faster than D-AMP as we will see in the experiments of visual comparisons. Note that, our method can be transformed to the standard AMP method by computing the parameters $c^{(0)}, c^{(1)}, \ldots, c^{(t-1)}$in Eq. (11) with the method of MC [24] and removing the acceleration steps.

TABLE 2. The PSNR (dB) results of different methods with 2D random subsampling scheme with varying amounts of additive white gaussian measurement noise.

Sampling rates	Sigma	Methods	PSNR							
			Chest	Shoulder	Brain1	Brain2	Brain3	Head	Brain4	Brain5
10%	10	ADMM-Net	23.23	29.81	28.07	27.83	29.16	25.20	27.69	28.19
		TGDOF	24.49	28.72	28.60	27.89	28.21	21.45	27.48	28.78
		PANO	22.93	28.36	27.59	28.52	29.20	21.75	28.05	28.97
		BM3D-IT	20.98	24.40	24.59	27.38	26.88	18.91	26.09	26.71
		BM3D-AMP-MRI	24.39	26.71	28.11	30.56	30.28	20.53	28.86	30.39
		NLR-CS	23.86	31.60	29.88	30.44	30.84	21.79	29.85	30.69
		D-AMP	23.49	26.17	27.67	29.71	29.96	20.60	28.45	29.43
		BM3DT-CS	24.80	30.87	28.22	29.69	30.16	22.66	28.44	30.43
		LT-CS	22.21	29.20	30.75	30.96	30.04	21.91	29.57	31.13
		ELT-CS	**24.90**	**30.93**	**30.76**	**30.99**	**31.00**	**22.65**	**29.91**	**31.59**
	20	ADMM-Net	20.71	25.17	23.93	23.73	24.37	21.30	23.64	24.35
		TGDOF	22.46	23.59	23.66	22.29	22.52	19.76	22.66	22.85
		PANO	21.69	25.15	25.03	25.08	25.74	21.26	24.94	25.82
		BM3D-IT	19.91	24.68	23.28	25.74	25.38	18.29	24.24	25.86
		BM3D-AMP-MRI	23.31	27.27	26.99	27.78	28.19	20.27	26.91	28.34
		NLR-CS	22.96	27.89	26.61	26.72	27.22	21.02	26.73	27.19
		D-AMP	22.71	26.87	26.47	27.92	28.59	20.32	27.22	28.11
		BM3DT-CS	23.53	29.69	26.52	27.70	28.61	21.46	27.24	28.48
		LT-CS	21.89	30.33	28.40	28.35	29.26	21.65	27.97	29.04
		ELT-CS	**23.47**	**30.58**	**28.75**	**29.02**	**29.39**	**21.34**	**28.36**	**29.60**
	30	ADMM-Net	18.51	22.08	20.89	21.00	21.15	18.58	20.55	21.21
		TGDOF	19.76	19.55	19.92	18.73	18.81	17.89	19.11	19.09
		PANO	21.02	22.76	22.83	21.84	23.02	19.83	22.53	22.48
		BM3D-IT	19.05	24.60	23.20	24.92	24.63	17.94	23.74	25.27
		BM3D-AMP-MRI	22.55	26.53	25.54	25.99	26.48	19.75	25.39	26.84
		NLR-CS	21.94	24.94	24.29	24.02	24.50	20.22	24.23	24.61
		D-AMP	21.77	27.05	25.67	26.52	27.53	20.30	26.34	27.26
		BM3DT-CS	21.57	28.78	25.25	26.09	27.33	21.32	25.74	27.31
		LT-CS	21.42	29.32	26.73	26.46	27.86	21.82	26.84	27.55
		ELT-CS	**22.45**	**29.81**	**27.14**	**27.41**	**28.09**	**21.12**	**27.02**	**27.91**
	40	ADMM-Net	17.40	20.17	19.12	19.04	18.79	16.94	18.71	19.63
		TGDOF	17.31	16.74	17.09	16.25	16.17	16.10	16.49	16.48
		PANO	20.11	20.46	20.99	19.83	20.97	18.43	20.73	20.52
		BM3D-IT	18.95	24.05	22.68	24.06	23.76	17.88	23.15	24.43
		BM3D-AMP-MRI	21.66	25.47	24.28	24.67	25.06	19.08	24.24	25.55
		NLR-CS	20.93	23.05	22.47	22.16	22.58	19.37	22.49	22.79
		D-AMP	21.17	27.03	24.69	25.31	26.65	19.97	25.20	26.53
		BM3DT-CS	20.91	27.52	24.40	25.31	26.59	20.21	24.94	26.49
		LT-CS	20.52	28.14	25.64	25.26	26.93	21.21	**25.87**	26.58
		ELT-CS	**21.71**	**28.40**	**25.80**	**26.26**	**27.15**	**20.45**	25.73	**26.95**
12%	10	ADMM-Net	25.14	30.62	28.04	28.70	28.65	26.75	27.17	28.91
		TGDOF	27.17	29.54	28.57	27.79	28.01	27.43	27.79	28.51
		PANO	25.28	31.65	27.69	28.35	28.82	26.13	27.54	29.23
		BM3D-IT	23.70	29.84	25.38	27.45	25.90	24.02	25.45	27.10
		BM3D-AMP-MRI	26.59	32.47	28.65	30.26	29.01	26.88	28.47	30.40
		NLR-CS	25.61	31.65	28.33	30.39	30.06	26.97	27.89	30.83
		D-AMP	26.85	33.32	28.27	29.42	29.19	26.96	28.26	29.68
		BM3DT-CS	26.11	33.75	29.41	30.00	30.97	27.71	30.05	31.52
		LT-CS	27.75	**35.00**	**31.63**	**31.42**	31.14	**28.96**	29.63	31.71
		ELT-CS	**28.06**	34.94	31.45	31.26	**31.43**	28.92	**30.36**	**32.07**
	20	ADMM-Net	22.30	25.42	23.50	24.08	24.18	22.97	23.19	24.54
		TGDOF	23.02	23.09	23.33	21.96	22.13	22.76	22.46	22.40
		PANO	23.51	26.36	25.20	24.88	25.33	24.05	24.59	25.66
		BM3D-IT	21.86	29.36	24.95	26.37	25.51	22.64	24.97	26.83
		BM3D-AMP-MRI	24.22	30.52	27.47	27.72	27.84	25.85	27.32	29.01
		NLR-CS	23.46	28.20	25.57	26.44	26.69	24.51	25.35	27.27
		D-AMP	24.36	32.14	27.18	27.99	28.61	26.19	27.54	29.00
		BM3DT-CS	23.75	31.85	27.50	28.08	29.09	26.28	28.38	29.48
		LT-CS	**26.04**	32.80	29.13	29.06	29.52	27.00	28.24	29.79
		ELT-CS	25.98	**32.89**	**29.44**	**29.37**	**29.89**	**27.15**	**28.66**	**30.32**

TABLE 2. *(Continued.)* **The PSNR (dB) results of different methods with 2D random subsampling scheme with varying amounts of additive white gaussian measurement noise.**

12%	30	ADMM-Net	20.30	22.32	21.20	21.00	21.16	20.38	20.30	21.52
		TGDOF	19.62	18.99	19.43	18.36	18.37	19.30	18.70	18.66
		PANO	22.03	23.12	22.87	21.74	22.60	22.39	22.11	22.32
		BM3D-IT	21.10	27.95	24.76	25.50	24.88	22.63	24.55	26.33
		BM3D-AMP-MRI	22.88	28.81	26.00	26.09	26.48	24.65	26.16	27.48
		NLR-CS	21.94	25.71	23.85	23.97	24.34	22.77	23.54	24.80
		D-AMP	23.26	30.54	26.37	26.92	27.55	25.31	26.77	28.04
		BM3DT-CS	22.36	30.10	26.65	26.22	27.86	24.75	26.86	28.00
		LT-CS	**24.45**	31.04	27.38	27.32	28.13	25.47	27.14	28.02
		ELT-CS	24.13	**31.28**	**27.82**	**27.77**	**28.44**	**25.64**	**27.34**	**28.69**
	40	ADMM-Net	18.76	20.24	19.39	19.19	18.91	18.63	18.54	19.52
		TGDOF	16.97	16.28	16.56	15.89	15.71	16.71	15.99	16.13
		PANO	20.78	20.55	20.88	19.81	20.50	20.06	20.35	20.11
		BM3D-IT	20.97	26.70	23.93	24.54	23.93	22.28	23.89	25.45
		BM3D-AMP-MRI	21.85	27.27	24.72	24.82	25.07	23.50	24.88	26.07
		NLR-CS	20.73	23.57	22.22	21.99	22.25	21.30	21.87	22.75
		D-AMP	22.23	29.51	25.65	25.48	27.04	24.38	25.91	27.11
		BM3DT-CS	21.82	29.35	25.71	25.46	27.08	24.06	25.90	27.11
		LT-CS	**23.25**	29.76	26.20	26.21	27.12	24.38	26.10	27.07
		ELT-CS	23.05	**30.07**	**26.62**	**26.47**	**27.40**	**24.50**	**26.28**	**27.58**
16%	10	ADMM-Net	27.96	31.07	29.51	29.42	29.48	28.16	29.07	30.01
		TGDOF	28.39	29.46	29.34	27.87	28.08	28.03	28.17	28.43
		PANO	28.16	32.45	30.35	29.94	30.60	28.51	29.81	30.76
		BM3D-IT	26.62	34.48	29.40	30.85	31.05	27.09	30.34	31.64
		BM3D-AMP-MRI	29.41	35.71	32.32	32.11	32.34	29.70	31.70	32.65
		NLR-CS	29.10	33.12	31.37	30.93	31.15	29.32	30.77	31.34
		D-AMP	29.96	36.49	32.57	31.90	32.38	29.47	31.88	32.70
		BM3DT-CS	29.96	36.21	32.49	31.76	32.19	29.43	31.74	32.53
		LT-CS	30.24	37.22	33.40	**32.89**	**33.06**	30.38	32.33	**33.24**
		ELT-CS	**30.65**	**37.29**	**33.48**	32.74	33.04	**30.41**	**32.44**	33.22
	20	ADMM-Net	23.65	25.36	24.58	24.30	24.29	23.79	24.19	24.81
		TGDOF	23.10	22.52	23.04	21.59	21.69	22.68	22.00	21.98
		PANO	25.25	26.19	26.25	25.41	25.67	25.56	25.55	26.05
		BM3D-IT	24.95	32.43	29.04	29.25	29.46	26.73	28.85	29.90
		BM3D-AMP-MRI	27.00	32.79	29.84	29.52	29.83	27.46	29.23	30.32
		NLR-CS	25.71	28.46	27.42	26.76	27.14	26.09	26.80	27.36
		D-AMP	27.46	33.69	30.18	29.55	30.29	27.62	29.67	30.51
		BM3DT-CS	27.37	33.25	30.00	29.43	30.17	27.52	29.57	30.33
		LT-CS	27.33	34.11	30.63	30.20	30.59	27.90	29.96	30.87
		ELT-CS	**28.02**	**34.28**	**30.76**	**30.24**	**30.80**	**28.10**	**30.11**	**30.98**
	30	ADMM-Net	21.01	22.20	21.66	21.29	21.18	20.92	21.20	21.71
		TGDOF	19.38	18.46	18.83	17.88	17.75	18.89	18.09	18.18
		PANO	23.07	22.50	23.19	21.70	22.44	22.40	22.55	22.04
		BM3D-IT	24.65	30.39	27.76	27.65	28.00	25.71	27.34	28.52
		BM3D-AMP-MRI	25.38	30.74	27.99	27.71	28.14	26.07	27.55	28.62
		NLR-CS	23.56	25.35	24.84	23.89	24.20	23.89	24.20	24.55
		D-AMP	25.87	31.91	28.63	28.12	28.96	26.48	28.26	29.13
		BM3DT-CS	25.69	31.22	28.33	27.95	28.70	26.23	27.98	28.89
		LT-CS	25.86	32.15	28.87	28.55	29.22	26.37	28.38	29.25
		ELT-CS	**26.28**	**32.39**	**29.03**	**28.66**	**29.37**	**26.71**	**28.52**	**29.46**
	40	ADMM-Net	19.14	19.95	19.55	19.21	18.94	18.89	19.00	19.55
		TGDOF	16.56	15.89	15.86	15.44	15.01	16.08	15.37	15.70
		PANO	20.31	19.96	20.75	19.48	20.09	20.40	20.20	19.52
		BM3D-IT	23.74	28.90	26.50	26.30	26.65	24.73	26.13	27.29
		BM3D-AMP-MRI	24.14	29.12	26.65	26.40	26.80	24.91	26.25	27.36
		NLR-CS	21.84	22.88	22.62	21.65	21.88	21.96	22.05	22.28
		D-AMP	24.41	30.76	27.41	26.93	27.98	25.41	27.10	28.13
		BM3DT-CS	24.26	30.77	27.24	26.83	27.79	25.30	26.94	27.95
		LT-CS	24.75	30.75	27.56	27.27	28.05	25.35	27.21	28.04
		ELT-CS	**25.02**	**31.19**	**27.82**	**27.48**	**28.34**	**25.78**	**27.42**	**28.40**

Visual comparisons between the reconstructions by different methods with measurement noises are provided in Figure 4, Figure 6, Figure 8 and Figure 10, while the corresponding iteration number vs. PSNR curves and CPU time vs. PSNR curves are presented in Figure 5 and Figure 7, Figure 9 and Figure 11 respectively. Figure 4 and

TABLE 3. The average SSIM results of different CS recovery methods with pseudo radial subsampling scheme.

Methods	SSIM											
	Sampling line = 20				Sampling line = 30				Sampling line = 40			
	$\sigma=10$	$\sigma=20$	$\sigma=30$	$\sigma=40$	$\sigma=10$	$\sigma=20$	$\sigma=30$	$\sigma=40$	$\sigma=10$	$\sigma=20$	$\sigma=30$	$\sigma=40$
ADMM-Net	0.6632	0.5490	0.4428	0.3512	0.7231	0.5720	0.4390	0.3347	0.7495	0.5719	0.4250	0.3197
TGDOF	0.6992	0.5685	0.4659	0.3833	0.7238	0.5578	0.4289	0.3388	0.7149	0.5204	0.3865	0.2901
PANO	0.6136	0.5073	0.4185	0.3582	0.6651	0.5227	0.4177	0.3385	0.6900	0.5223	0.4053	0.3247
BM3D-IT	0.6763	0.6769	0.6514	0.6211	0.7764	0.7468	0.7039	0.6604	0.8262	0.7789	0.7268	0.6806
BM3D-AMP-MRI	0.7397	0.7043	0.6656	0.6322	0.8067	0.7565	0.7074	0.6632	0.8395	0.7805	0.7257	0.6788
NLR-CS	0.6023	0.5269	0.4353	0.3543	0.6921	0.5508	0.4316	0.3414	0.7102	0.5468	0.4196	0.3280
D-AMP	0.7398	0.7140	0.6895	0.6658	0.8114	0.7683	0.7340	0.7002	0.8446	0.7954	0.7549	0.7161
BM3DT-CS	0.7431	0.7080	0.6764	0.6597	0.8099	0.7603	0.7175	0.6872	0.8423	0.7829	0.7321	0.6974
LT-CS	0.7617	0.7231	0.6863	0.6455	0.8322	0.7748	0.7299	0.6837	0.8620	0.8076	0.7533	0.6993
ELT-CS	**0.7815**	**0.7416**	**0.7071**	**0.6722**	**0.8354**	**0.7884**	**0.7489**	**0.7106**	**0.8647**	**0.8155**	**0.7679**	**0.7265**

TABLE 4. The average SSIM results of different CS recovery methods with 2D random subsampling scheme.

Methods	SSIM											
	Sampling rate = 10%				Sampling rate = 20%				Sampling rate = 30%			
	$\sigma=10$	$\sigma=20$	$\sigma=30$	$\sigma=40$	$\sigma=10$	$\sigma=20$	$\sigma=30$	$\sigma=40$	$\sigma=10$	$\sigma=20$	$\sigma=30$	$\sigma=40$
ADMM-Net	0.6871	0.4698	0.3205	0.2305	0.6955	0.4612	0.3122	0.2237	0.7087	0.4552	0.3063	0.2205
TGDOF	0.6583	0.4351	0.2937	0.2042	0.6700	0.4127	0.2654	0.1790	0.6524	0.3792	0.2367	0.1591
PANO	0.6874	0.5368	0.4234	0.3405	0.7109	0.5410	0.4191	0.3342	0.7368	0.5443	0.4123	0.3197
BM3D-IT	0.6161	0.5569	0.5225	0.4866	0.6918	0.6353	0.5876	0.5354	0.8173	0.7534	0.6836	0.6183
BM3D-AMP-MRI	0.7457	0.6694	0.5934	0.5295	0.7943	0.7042	0.6224	0.5493	0.8572	0.7648	0.6839	0.6181
NLR-CS	0.7487	0.6221	0.4976	0.3955	0.7745	0.6046	0.4539	0.3485	0.7974	0.5925	0.4421	0.3392
D-AMP	0.7328	0.6914	0.6526	0.6196	0.7981	0.7475	0.6944	0.6489	0.8727	0.8018	0.7411	0.6944
BM3DT-CS	0.7599	0.7000	0.6511	0.6128	0.8121	0.7375	0.6765	0.6385	0.8657	0.7884	0.7137	0.6800
LT-CS	0.7428	0.7052	0.6434	0.5956	0.8357	0.7623	0.6862	0.6355	0.8886	0.8174	0.7482	0.6804
ELT-CS	**0.7906**	**0.7412**	**0.6845**	**0.6431**	**0.8426**	**0.7891**	**0.7240**	**0.6761**	**0.8911**	**0.8263**	**0.7669**	**0.7164**

Figure 8 show the performance comparisons of competing methods with the standard deviation of noise i.e. sigma=10 and sigma=20 representing the lower-power noise environment, while Figure 6 and Figure 10 show the ones with sigma=30 and sigma=40 representing the higher-power noise environment. From these figures, we can clearly see that the proposed algorithm ELT-CS performs better than others, which enjoys great advantages in producing clearer images, e.g. in the edges of the organ and blood-vessels. Generally, the reconstructed images of ELT-CS deliver excellent image contrast and clear details due to its capability of achieving a better spatial adaptation using complementary regularizers and side information. On contrast, reconstructed images by ADMM-Net, TGDOF, PANO and NLR-CS all suffer from noticeable noise spots, meaning that they are sensitive to noise. BM3D-IT, BM3D-AMP-MRI, D-AMP, BM3DT-CS and LT-CS have a certain anti-noise ability, however, the images reconstructed by the former four methods are over-smoothed when compared to the one by ELT-CS, resulting in a lack of image details, while the one reconstructed by LT-CS has poor image contrast and visual artifacts. These results verify again that the combination of Laplacian-scaled thresholding and BM3D thresholding is reasonable.

The CPU time and PSNR are traced in each iteration for each of reconstruction methods. The simulations were executed in Matlab on a computer with an Intel i7 CPU at 2.6GHz, 16GB memory and 64-bit operating system. None of comparison algorithms uses parallelization or GPU. Figure 5 (a), 7 (a), 9 (a), 11 (a) and Figure 5 (b), 7 (b), 9 (b), 11 (b) present the iteration number vs. PSNR curves

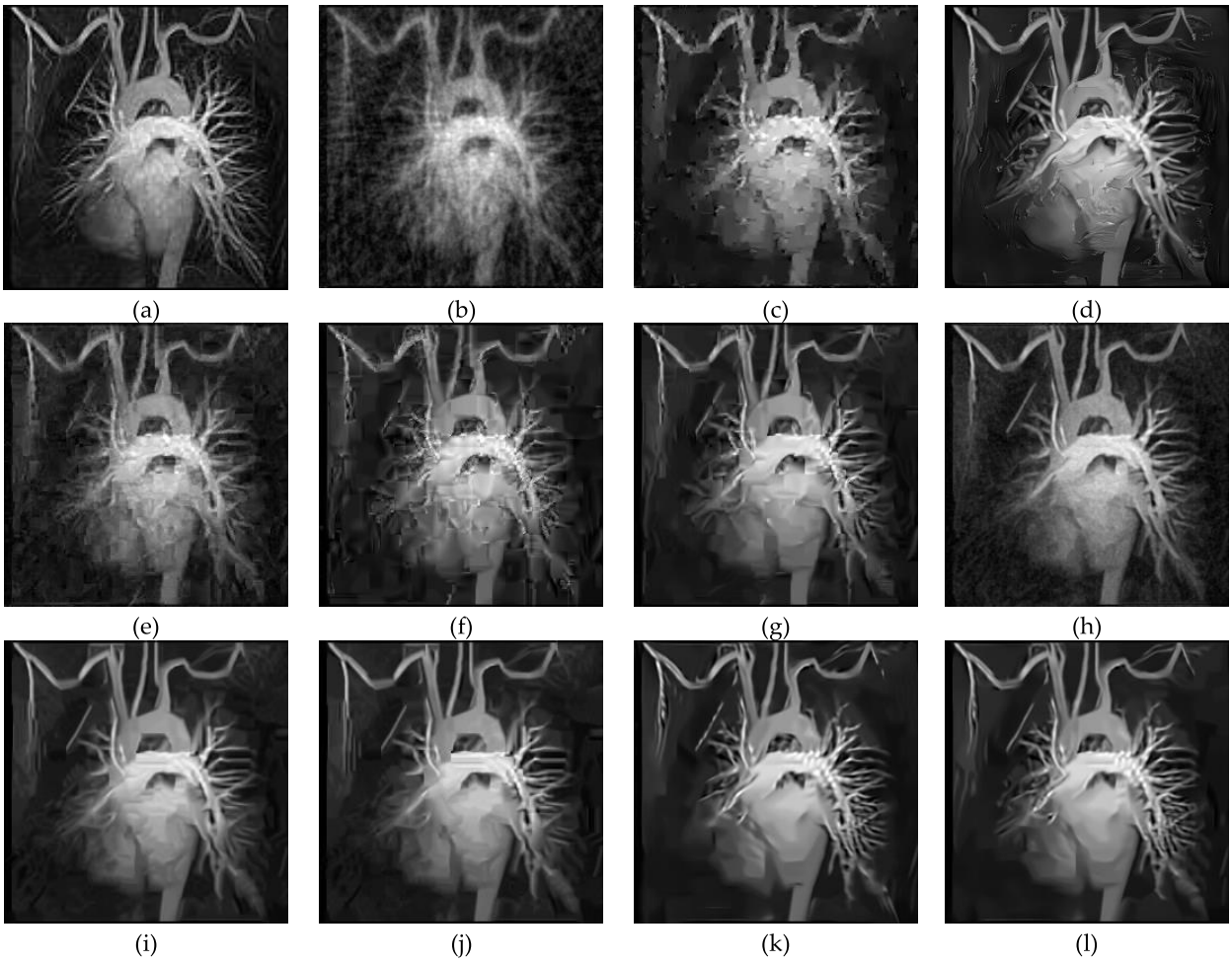

FIGURE 4. Visual comparisons on Chest image using 30 sampling lines (pseudo radial) with measurement noise with standard deviation 10 (i.e. SNR: 25.41 dB): (a) Original; (b) Zero-filling (c) ADMM-Net (PSNR: 23.45 dB, SSIM: 0.5951); (d) TGDOF (PSNR: 25.00 dB, SSIM: 0.6578); (e) PANO (PSNR: 23.41 dB, SSIM: 0.5782) (f) BM3D-IT (PSNR: 23.17 dB, SSIM: 0.5831) (g) BM3D-AMP-MRI (PSNR: 24.59 dB, SSIM: 0.6513) (h) NLR-CS (PSNR: 24.80 dB, SSIM: 0.6318); (i) D-AMP (PSNR: 24.89 dB, SSIM: 0.6561); (j) BM3DT-CS (PSNR: 24.77 dB, SSIM: 0.6478); (k) LT-CS (PSNR: 24.91 dB, SSIM: 0.6718), (l) ELT-CS (PSNR: 25.46 dB, SSIM: 0.6864).

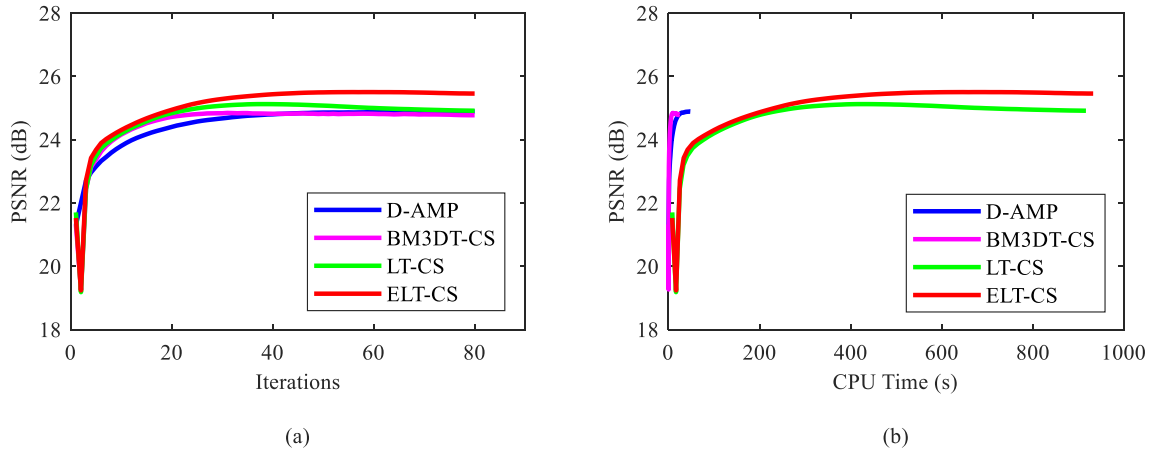

FIGURE 5. Iterative curves on Chest image using 30 sampling lines (pseudo radial) with measurement noise with standard deviation 10 (i.e. SNR: 25.41 dB): (a) Average PSNR to iterations; (b) Average PSNR to CPU time.

and CPU time vs. PSNR curves respectively. Because the codes of some algorithms used for comparison including the ones of PANO, BM3D-IT and BM3D-AMP-MRI have been encapsulated, meanwhile, deep learning-based methods have no iterations, we only present the results of D-AMP, BM3DT-CS, LT-CS and ELT-CS. ELT-CS achieves the best

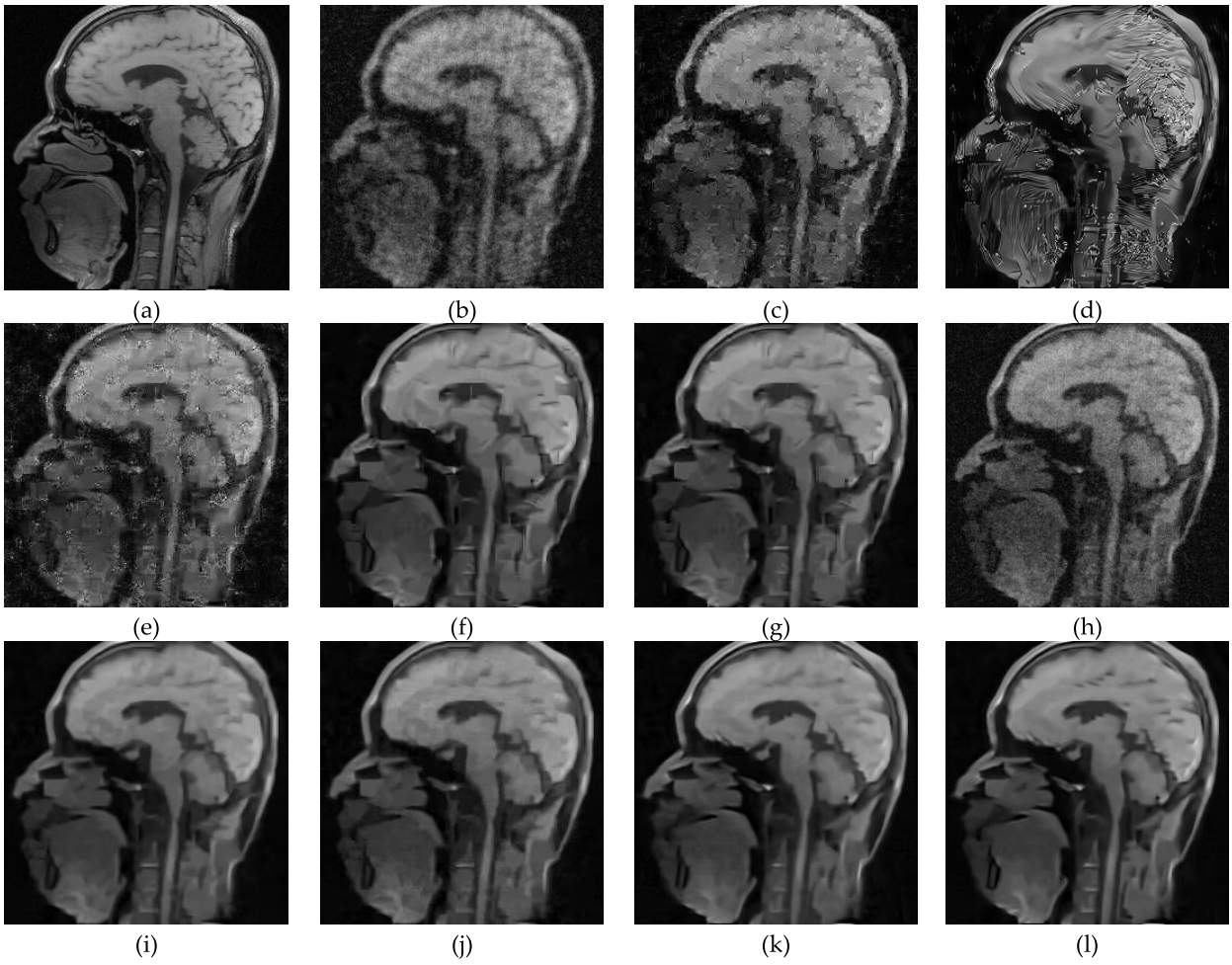

FIGURE 6. Visual comparisons on Head image using 40 sampling lines (pseudo radial) with measurement noise with standard deviation 30 (i.e. SNR: 14.70 dB): (a) Original; (b) Zero-filling (c) ADMM-Net (PSNR: 22.95 dB, SSIM: 0.4648); (d) TGDOF (PSNR: 20.20 dB, SSIM: 0.4667); (e) PANO (PSNR: 21.84 dB, SSIM: 0.4515) (f) BM3D-IT (PSNR: 25.71 dB, SSIM: 0.6793) (g) BM3D-AMP-MRI (PSNR: 25.74 dB, SSIM: 0.6784) (h) NLR-CS (PSNR: 23.80 dB, SSIM: 0.4773); (i) D-AMP (PSNR: 25.78 dB, SSIM: 0.6889); (j) BM3DT-CS (PSNR: 25.63 dB, SSIM: 0.6741); (k) LT-CS (PSNR: 26.24 dB, SSIM: 0.7008), (l) ELT-CS (PSNR: 26.33 dB, SSIM: 0.7099).

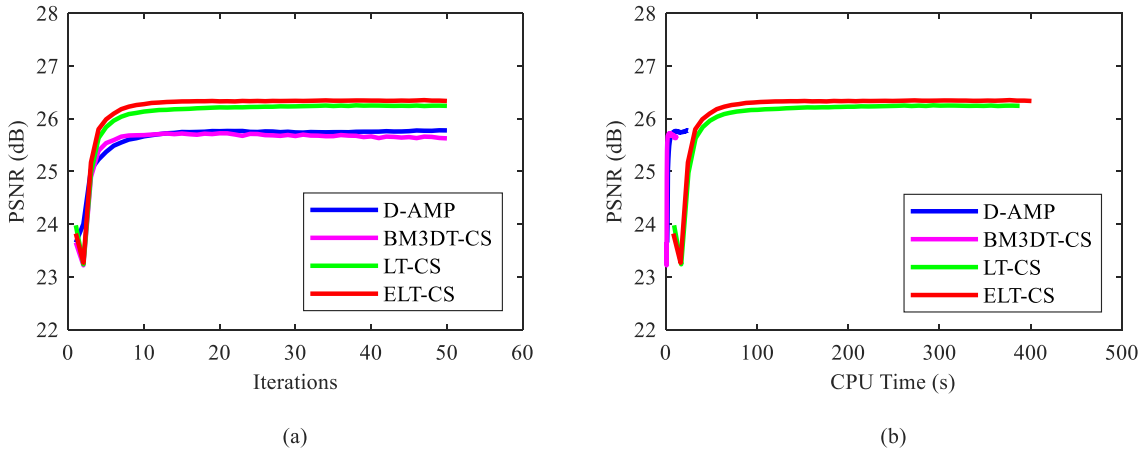

FIGURE 7. Iterative curves on Head image using 40 sampling lines (pseudo radial) with measurement noise with standard deviation 30 (i.e. SNR: 14.70 dB): (a) Average PSNR to iterations; (b) Average PSNR to CPU time.

performance in terms of PSNR and CPU time after about 30 iterations in Figure 5 (a) and after about 200 seconds in Figure 5 (b). These curves validate that the proposed method ELT-CS can converge to a good reconstructed result in a reasonable amount of time. The average CPU time to reconstruct a MR image with size of 256 × 256 by

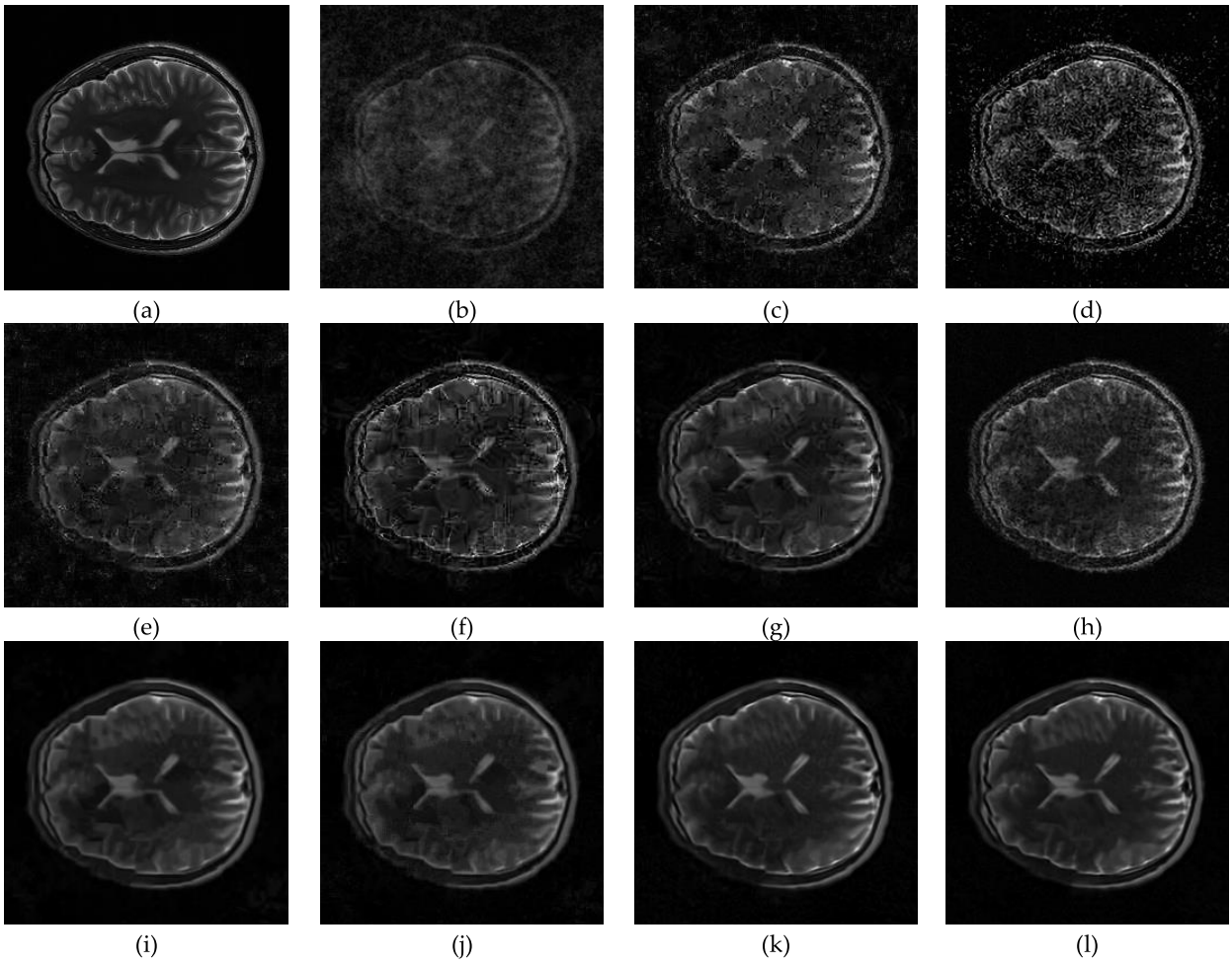

FIGURE 8. Visual comparisons on Brain2 image at 10% sampling ratio (2D random) with measurement noise with standard deviation 20 (i.e. SNR: 12.09 dB): (a) Original; (b) Zero-filling (c) ADMM-Net (PSNR: 23.73 dB, SSIM: 0.4131); (d) TGDOF (PSNR: 22.29 dB, SSIM: 0.4369); (e) PANO (PSNR: 25.08 dB, SSIM: 0.4821) (f) BM3D-IT (PSNR: 25.74 dB, SSIM: 0.6530) (g) BM3D-AMP-MRI (PSNR: 27.78 dB, SSIM: 0.7239) (h) NLR-CS (PSNR: 26.72 dB, SSIM: 0.6127); (i) D-AMP (PSNR: 27.92 dB, SSIM: 0.7831); (j) BM3DT-CS (PSNR: 27.70 dB, SSIM: 0.7482); (k) LT-CS (PSNR: 28.35 dB, SSIM: 0.7175), (l) ELT-CS (PSNR: 29.02 dB, SSIM: 0.7909).

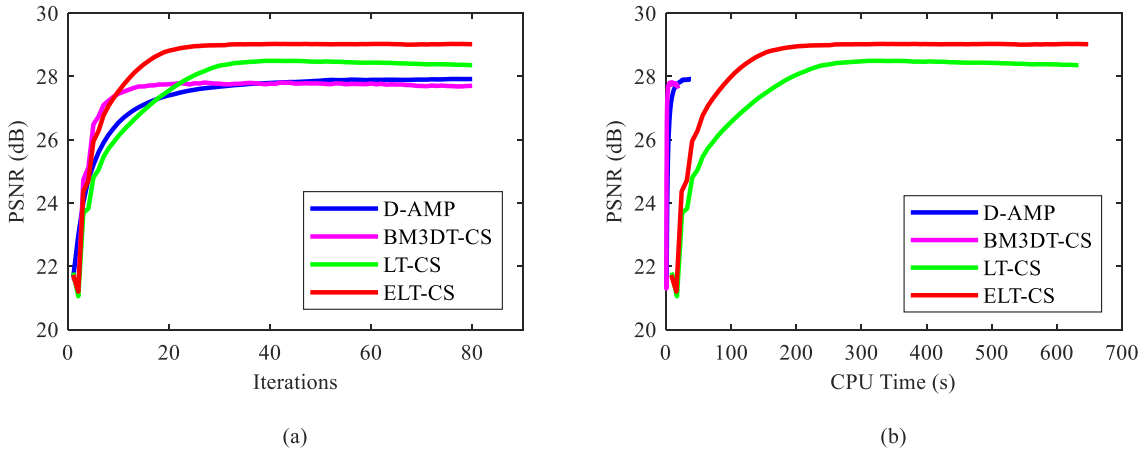

FIGURE 9. Iterative curves on Brain2 image at 10% sampling ratio (2D random) with measurement noise with standard deviation 20 (i.e. SNR: 12.09 dB): (a) Average PSNR to iterations; (b) Average PSNR to CPU time.

ADMM-Net, TGDOF, PANO, BM3D-IT, BM3D-AMP-MRI, NLR-CS, D-AMP, BM3DT-CS, LT-CS and ELT-CS are about 3.41 s, 89.91 s, 151.54 s, 8.14 s, 14.89 s, 761.60 s, 27.73 s, 13.85 s, 461.32 s and 474.34 s, respectively. Note that, the last three methods can converge with 13.85 s, 461.32 s and 474.34 s (i.e. with about 50 iterations) in

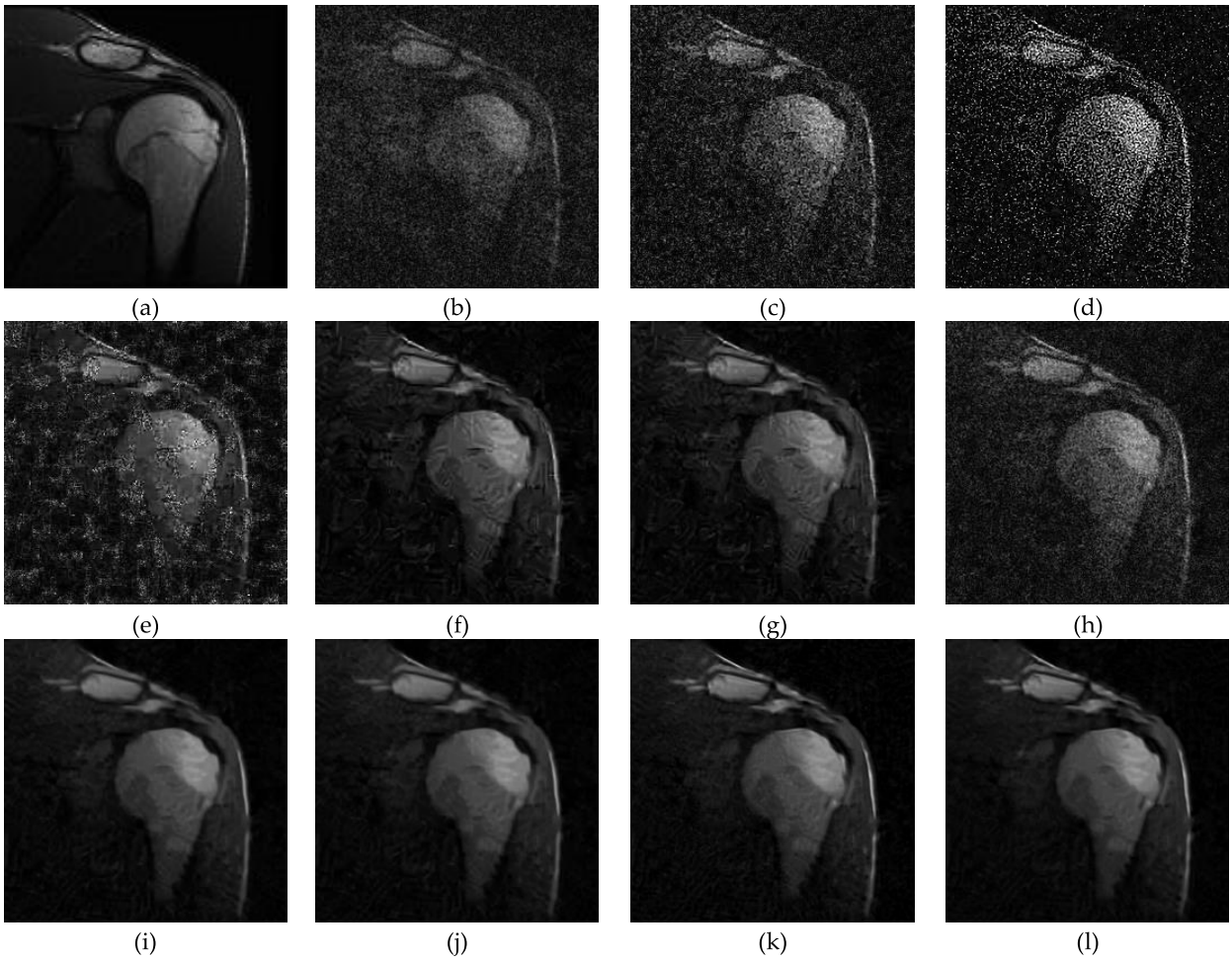

FIGURE 10. Visual comparisons on Shoulder image at 16% sampling ratio (2D random) with measurement noise with standard deviation 40 (i.e. SNR: 4.15 dB): (a) Original; (b) Zero-filling (c) ADMM-Net (PSNR: 19.95 dB, SSIM: 0.1661); (d) TGDOF (PSNR: 15.89 dB, SSIM: 0.1064); (e) PANO (PSNR: 19.96 dB, SSIM: 0.2922) (f) BM3D-IT (PSNR: 28.90 dB, SSIM: 0.6710) (g) BM3D-AMP-MRI (PSNR: 29.12 dB, SSIM: 0.6732) (h) NLR-CS (PSNR: 22.88 dB, SSIM: 0.2929); (i) D-AMP (PSNR: 30.76 dB, SSIM: 0.7869); (j) BM3DT-CS (PSNR: 30.77 dB, SSIM: 0.7879); (k) LT-CS (PSNR: 30.75 dB, SSIM: 0.7416), (l) ELT-CS (PSNR: 31.19 dB, SSIM: 0.7973).

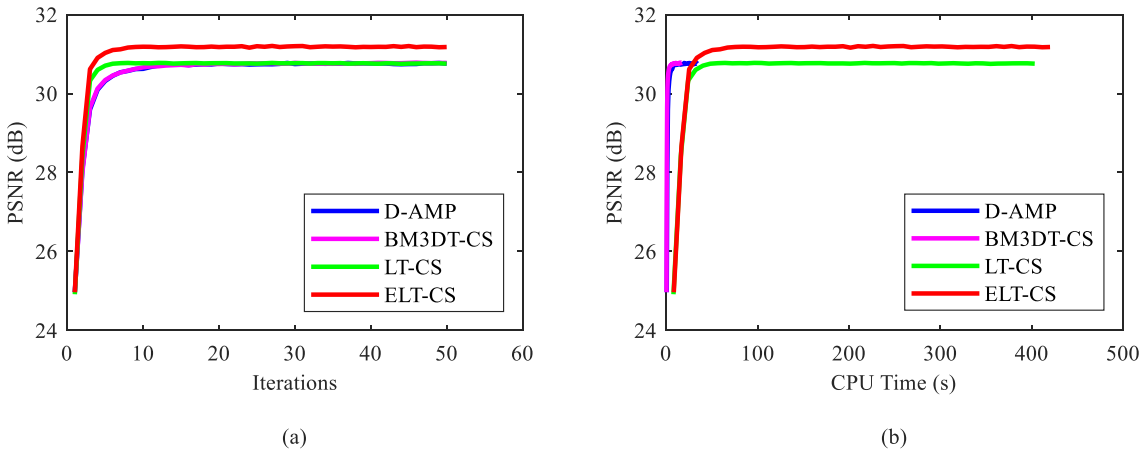

FIGURE 11. Iterative curves on Shoulder image at 16% sampling ratio (2D random) with measurement noise with standard deviation 40 (i.e. SNR: 4.15 dB): (a) Average PSNR to iterations; (b) Average PSNR to CPU time.

lower-power noise environment and with 5.96 s, 178.68 s, 183.13 s (i.e. with about 20 iterations) in the higher one, respectively. The deep learning method ADMM-Net is fast, which takes only several seconds to reconstruct an image, but it spends a lot of time to train a deep learning network, meanwhile they are sensitive to noise. Most of comparison methods

TABLE 5. The PSNR (dB) results of different methods with noiseless measurements.

Sampling methods	Sampling rates	Methods	PSNR							
			Chest	Shoulder	Brain1	Brain2	Brain3	Head	Brain4	Brain5
2D random	10%	ADMM-Net	21.56	32.98	26.52	26.85	28.29	23.57	25.57	29.58
		TGDOF	22.88	34.14	**29.59**	29.89	30.75	**25.67**	29.14	31.18
		PANO	21.66	32.07	25.93	27.22	27.85	23.34	26.00	29.27
		BM3D-IT	21.16	29.14	24.28	26.32	26.55	22.30	25.08	27.46
		BM3D-AMP-MRI	22.00	32.47	27.38	29.01	29.06	23.97	27.65	30.45
		NLR-CS	22.78	31.91	27.89	28.24	28.99	24.64	27.88	29.10
		D-AMP	22.50	32.57	27.35	29.07	30.08	24.16	28.24	30.35
		BM3DT-CS	22.96	35.09	28.75	29.24	29.74	24.98	28.82	30.38
		LT-CS	22.75	35.16	29.18	30.69	31.40	25.07	30.04	31.23
		ELT-CS	**23.34**	**35.46**	29.41	**30.87**	**31.57**	25.48	**30.18**	**31.53**
	12%	ADMM-Net	24.00	35.93	29.98	29.86	31.08	26.02	29.37	31.92
		TGDOF	**26.20**	37.43	31.92	32.94	33.42	**28.26**	31.55	33.46
		PANO	23.78	35.27	29.15	29.68	30.69	25.66	29.24	31.54
		BM3D-IT	22.73	31.36	26.30	28.30	28.72	24.26	27.35	29.03
		BM3D-AMP-MRI	24.46	35.31	30.03	31.53	31.68	26.56	30.53	32.47
		NLR-CS	25.77	36.32	31.73	32.00	32.72	28.19	31.57	32.53
		D-AMP	25.14	36.05	31.09	32.70	32.69	27.40	31.68	33.17
		BM3DT-CS	25.53	38.26	31.57	33.21	32.85	27.37	31.41	33.26
		LT-CS	25.25	38.89	31.89	33.53	34.38	27.91	32.25	33.35
		ELT-CS	25.93	**38.97**	**32.04**	**33.79**	**34.44**	28.15	**32.40**	**33.54**
	16%	ADMM-Net	25.79	38.63	32.39	32.12	33.37	28.20	31.94	33.83
		TGDOF	28.25	39.23	33.68	34.65	35.04	29.85	33.12	34.94
		PANO	25.84	38.21	31.52	32.03	32.84	27.68	31.48	33.49
		BM3D-IT	24.31	33.28	28.11	30.06	30.48	26.03	29.37	30.57
		BM3D-AMP-MRI	26.25	37.55	31.95	33.60	33.74	28.39	32.47	34.10
		NLR-CS	28.30	38.02	33.45	33.61	33.93	29.89	33.08	33.92
		D-AMP	27.05	38.31	32.88	34.40	34.66	29.28	33.32	34.40
		BM3DT-CS	27.71	40.14	33.63	35.09	35.12	29.62	33.72	34.84
		LT-CS	28.04	40.84	34.14	35.40	35.73	30.26	34.20	35.20
		ELT-CS	**28.39**	**40.86**	**34.22**	**35.54**	**35.79**	**30.34**	**34.29**	**35.23**
Radial	20 lines	ADMM-Net	21.56	32.98	26.52	26.85	28.29	23.57	25.57	29.58
		TGDOF	22.88	34.14	**29.59**	29.89	30.75	**25.67**	29.14	31.18
		PANO	21.66	32.07	25.93	27.22	27.85	23.34	26.00	29.27
		BM3D-IT	21.16	29.14	24.28	26.32	26.55	22.30	25.08	27.46
		BM3D-AMP-MRI	22.00	32.47	27.38	29.01	29.06	23.97	27.65	30.45
		NLR-CS	22.78	31.91	27.89	28.24	28.99	24.64	27.88	29.10
		D-AMP	22.50	32.57	27.35	29.07	30.08	24.16	28.24	30.35
		BM3DT-CS	22.96	35.09	28.75	29.24	29.74	24.98	28.82	30.38
		LT-CS	22.75	35.16	29.18	30.69	31.40	25.07	30.04	31.23
		ELT-CS	**23.34**	**35.46**	29.41	**30.87**	**31.57**	25.48	**30.18**	**31.53**
	30 lines	ADMM-Net	24.00	35.93	29.98	29.86	31.08	26.02	29.37	31.92
		TGDOF	**26.20**	37.43	31.92	32.94	33.42	**28.26**	31.55	33.46
		PANO	23.78	35.27	29.15	29.68	30.69	25.66	29.24	31.54
		BM3D-IT	22.73	31.36	26.30	28.30	28.72	24.26	27.35	29.03
		BM3D-AMP-MRI	24.46	35.31	30.03	31.53	31.68	26.56	30.53	32.47
		NLR-CS	25.77	36.32	31.73	32.00	32.72	28.19	31.57	32.53
		D-AMP	25.14	36.05	31.09	32.70	32.69	27.40	31.68	33.17
		BM3DT-CS	25.53	38.26	31.57	33.21	32.85	27.37	31.41	33.26
		LT-CS	25.25	38.89	31.89	33.53	34.38	27.91	32.25	33.35
		ELT-CS	25.93	**38.97**	**32.04**	**33.79**	**34.44**	28.15	**32.40**	**33.54**
	40 lines	ADMM-Net	25.79	38.63	32.39	32.12	33.37	28.20	31.94	33.83
		TGDOF	28.25	39.23	33.68	34.65	35.04	29.85	33.12	34.94
		PANO	25.84	38.21	31.52	32.03	32.84	27.68	31.48	33.49
		BM3D-IT	24.31	33.28	28.11	30.06	30.48	26.03	29.37	30.57
		BM3D-AMP-MRI	26.25	37.55	31.95	33.60	33.74	28.39	32.47	34.10
		NLR-CS	28.30	38.02	33.45	33.61	33.93	29.89	33.08	33.92
		D-AMP	27.05	38.31	32.88	34.40	34.66	29.28	33.32	34.40
		BM3DT-CS	27.71	40.14	33.63	35.09	35.12	29.62	33.72	34.84
		LT-CS	28.04	40.84	34.14	35.40	35.73	30.26	34.20	35.20
		ELT-CS	**28.39**	**40.86**	**34.22**	**35.54**	**35.79**	**30.34**	**34.29**	**35.23**

are based on BM3D denoiser which is written in C language, thus have a faster speed than the methods including NLR-CS, LT-CS and ELT-CS that use pure MATLAB implementation without a C-coded optimization. Our ELT-CS method

converges reasonably fast among the ones with pure MATLAB implementation due to the acceleration steps derived from FISTA.

B. EXPERIMENTS ON NOISELESS MEASUREMENTS

Although we focus on the problem of robustness to noise in this work, we still conduct the reconstruction experiments by all comparison algorithms with noiseless measurements. Because of space limitations, we only present the PSNR results of these methods with different sampling masks, sampling rates and test images which are shown in Table 5. From Table 5, one can clearly see that our method ELT-CS still achieves the best PSNR results on average, while the deep learning-based method TGDOF is sometimes better than ELT-CS. Deep learning-based methods ADMM-Net and TGDOF perform much better in the noiseless environment. Furthermore, the differences of performance of algorithms are reduced when compared to the ones with noisy measurements. These results demonstrate that the proposed method ELT-CS has the superiority in reconstructing MR images when there exists no external noise.

V. CONCLUSION

We have proposed an effective iterative algorithm with enhanced Laplacian-scaled thresholding for noise-robust CS-MRI. Our work has the following contributions. First, guided by information and structural sparsity theories, we introduce the use of complementary regularizers and side information to Laplacian-scaled model in CS-MRI, and provide a plug-and-play prior method to formulate composite sparse problem combining with the nonlocal sparsity in spatial and frequency domain. It can substantially enhance the robustness to noise for CS-MRI. Second, an efficient AMP-like algorithm with excellent reconstruction quality and fast convergence performance is proposed in this paper to solve this model. These properties make the CS-MRI much more reliable than before. Finally, our simulations and experiments on MR images demonstrate the superiority of the proposed algorithm in robustness to the state-of-the-art nonlocal sparsity-based CS-MRI algorithms and two deep learning-based algorithms in CS-MRI. While this work has designed a flexible iterative method for using composite sparse models in CS image reconstruction, and demonstrated the promise of combining two nonlocal sparsity, we plan to systematically study the combination of deep learning-based priors and nonlocal regularizers in inverse problems in future work. Furthermore, in order to enable our model to be used in practical MRI systems, we plan to define the complex-valued Laplacian-scaled thresholding operator in the frame of the complex version of AMP.

REFERENCES

[1] K. Scheffler, A. Loktyushin, J. Bause, A. Aghaeifar, T. Steffen, and B. Schölkopf, "Spread–spectrum magnetic resonance imaging," *Magn. Reson. Med.*, vol. 52, pp. 877–885, Apr. 2019.

[2] D. L. Donoho, "Compressed sensing," *IEEE Trans. Inf. Theory*, vol. 52, no. 4, pp. 1289–1306, Apr. 2006.

[3] C. Gan, X. Yan, Y. Wu, and Z. Zhang, "A two-branch convolution residual network for image compressive sensing," *IEEE Access*, vol. 8, pp. 1705–1714, 2020.

[4] Y. Liu, Q. Liu, M. Zhang, Q. Yang, S. Wang, and D. Liang, "IFR-net: Iterative feature refinement network for compressed sensing MRI," *IEEE Trans. Comput. Imag.*, vol. 6, no. 5, pp. 434–446, Nov. 2020.

[5] Z. Xie, L. Liu, and C. Yang, "A probabilistic model-based method with nonlocal filtering for robust magnetic resonance imaging reconstruction," *IEEE Access*, vol. 8, pp. 82347–82363, 2020.

[6] M. Usman, C. Prieto, F. Odille, D. Atkinson, T. Schaeffter, and P. G. Batchelor, "A computationally efficient OMP-based compressed sensing reconstruction for dynamic MRI," *Phys. Med. Biol.*, vol. 56, no. 7, pp. 99–114, Mar. 2011.

[7] A. Beck and M. Teboulle, "A fast iterative shrinkage-thresholding algorithm for linear inverse problems," *SIAM J. Imag. Sci.*, vol. 2, no. 1, pp. 183–202, Jan. 2009.

[8] C. Chen and J. Huang, "The benefit of tree sparsity in accelerated MRI," *Med. Image Anal.*, vol. 18, no. 6, pp. 834–842, Aug. 2014.

[9] J. Assländer, M. A. Cloos, F. Knoll, D. K. Sodickson, J. Hennig, and R. Lattanzi, "Low rank alternating direction method of multipliers reconstruction for MR fingerprinting," *Magn. Reson. Med.*, vol. 79, no. 1, pp. 83–96, Jan. 2018.

[10] W. Yin, S. Osher, D. Goldfarb, and J. Darbon, "Bregman iterative algorithms for ℓ_1-minimization with applications to compressed sensing," *SIAM J. Imag. Sci.*, vol. 1, no. 1, pp. 143–168, Jan. 2008.

[11] S. Liu, Y. D. Zhang, T. Shan, and R. Tao, "Structure-aware Bayesian compressive sensing for frequency-hopping spectrum estimation with missing observations," *IEEE Trans. Signal Process.*, vol. 66, no. 8, pp. 2153–2166, Apr. 2018.

[12] D. L. Donoho, A. Maleki, and A. Montanari, "Message passing algorithms for compressed sensing: II. Analysis and validation," in *Proc. IEEE Inf. Theory Workshop (ITW)*, Cairo, Egypt, Jan. 2010, pp. 1–5.

[13] S. Som and P. Schniter, "Compressive imaging using approximate message passing and a Markov-tree prior," *IEEE Trans. Signal Process.*, vol. 60, no. 7, pp. 3439–3448, Jul. 2012.

[14] Y. Chen, Y. Lou, K. Wang, M. A. Kupinski, and M. A. Anastasio, "Reconstruction-aware imaging system ranking by use of a sparsity-driven numerical observer enabled by variational Bayesian inference," *IEEE Trans. Med. Imag.*, vol. 38, no. 5, pp. 1251–1262, May 2019.

[15] S. Ma, W. Yin, Y. Zhang, and A. Chakraborty, "An efficient algorithm for compressed MR imaging using total variation and wavelets," in *Proc. IEEE Conf. Comput. Vis. Pattern Recognit.*, Anchorage, AK, USA, Jun. 2008, pp. 1–8.

[16] S. Ravishankar and Y. Bresler, "MR image reconstruction from highly undersampled k-Space data by dictionary learning," *IEEE Trans. Med. Imag.*, vol. 30, no. 5, pp. 1028–1041, May 2011.

[17] C. Chen and J. Huang, "Exploiting the wavelet structure in compressed sensing MRI," *Magn. Reson. Imag.*, vol. 32, no. 10, pp. 1377–1389, Dec. 2014.

[18] S. Liu, "Group sparsity with orthogonal dictionary and nonconvex regularization for exact MRI reconstruction," *Inf. Sci.*, vol. 451, pp. 161–179, Jul. 2018.

[19] Z. Xie, L. Liu, and C. Yang, "An entropy-based algorithm with nonlocal residual learning for image compressive sensing recovery," *Entropy*, vol. 21, no. 9, p. 900, Sep. 2019.

[20] D. Liang, H. Wang, Y. Chang, and L. Ying, "Sensitivity encoding reconstruction with nonlocal total variation regularization," *Magn. Reson. Med.*, vol. 65, no. 5, pp. 1384–1392, May 2011.

[21] X. Qu, Y. Hou, F. Lam, D. Guo, J. Zhong, and Z. Chen, "Magnetic resonance image reconstruction from undersampled measurements using a patch-based nonlocal operator," *Med. Image Anal.*, vol. 18, no. 6, pp. 843–856, Aug. 2014.

[22] W. Dong, G. Shi, X. Li, Y. Ma, and F. Huang, "Compressive sensing via nonlocal low-rank regularization," *IEEE Trans. Image Process.*, vol. 23, no. 8, pp. 3618–3632, Aug. 2014.

[23] K. Dabov, A. Foi, V. Katkovnik, and K. Egiazarian, "Image denoising by sparse 3-D transform-domain collaborative filtering," *IEEE Trans. Image Process.*, vol. 16, no. 8, pp. 2080–2095, Aug. 2007.

[24] C. A. Metzler, A. Maleki, and R. G. Baraniuk, "From denoising to compressed sensing," *IEEE Trans. Inf. Theory*, vol. 62, no. 9, pp. 5117–5144, Sep. 2016.

[25] E. M. Eksioglu, "Decoupled algorithm for MRI reconstruction using nonlocal block matching model: BM3D-MRI," *J. Math. Imag. Vis.*, vol. 56, no. 3, pp. 430–440, Mar. 2016.

[26] E. M. Eksioglu and A. K. Tanc, "Denoising AMP for MRI reconstruction: BM3D-AMP-MRI," *SIAM J. Imag. Sci.*, vol. 11, no. 3, pp. 2090–2109, Jan. 2018.
[27] J. Yao, Z. Xu, X. Huang, and J. Huang, "An efficient algorithm for dynamic MRI using low-rank and total variation regularizations," *Med. Image Anal.*, vol. 44, pp. 14–27, Feb. 2018.
[28] S. Ravishankar, B. E. Moore, R. R. Nadakuditi, and J. A. Fessler, "Low-rank and adaptive sparse signal (LASSI) models for highly accelerated dynamic imaging," *IEEE Trans. Med. Imag.*, vol. 36, no. 5, pp. 1116–1128, May 2017.
[29] B. Wen, Y. Li, and Y. Bresler, "Image recovery via transform learning and low-rank modeling: The power of complementary regularizers," *IEEE Trans. Image Process.*, vol. 29, pp. 5310–5323, Mar. 2020.
[30] B. Zhu, J. Z. Liu, S. F. Cauley, B. R. Rosen, and M. S. Rosen, "Image reconstruction by domain-transform manifold learning," *Nature*, vol. 555, no. 7697, pp. 487–492, Mar. 2018.
[31] M. Mardani, E. Gong, J. Y. Cheng, S. S. Vasanawala, G. Zaharchuk, L. Xing, and J. M. Pauly, "Deep generative adversarial neural networks for compressive sensing MRI," *IEEE Trans. Med. Imag.*, vol. 38, no. 1, pp. 167–179, Jan. 2019.
[32] Y. Yang, J. Sun, H. Li, and Z. Xu, "ADMM-CSNet: A deep learning approach for image compressive sensing," *IEEE Trans. Pattern Anal. Mach. Intell.*, vol. 42, no. 3, pp. 521–538, Mar. 2020.
[33] J. Zhang and B. Ghanem, "ISTA-net: Interpretable optimization-inspired deep network for image compressive sensing," in *Proc. IEEE/CVF Conf. Comput. Vis. Pattern Recognit.*, Salt Lake City, Utah, USA, Jun. 2018, pp. 1828–1837.
[34] C. A. Metzler, A. Mousavi, and R. G. Baraniuk, "Learned D-AMP: Principled neural network based compressive image recovery," 2017, *arXiv:1704.06625*. [Online]. Available: http://arxiv.org/abs/1704.06625
[35] P. Garrigues and B. A. Olshausen, "Group sparse coding with a Laplacian scale mixture prior," in *Proc. Adv. Neural Inf. Process. Syst. (NIPS)*, Vancouver, BC, Canada, Dec. 2010, pp. 676–684.
[36] W. Dong, T. Huang, G. Shi, Y. Ma, and X. Li, "Robust tensor approximation with Laplacian scale mixture modeling for multiframe image and video denoising," *IEEE J. Sel. Topics Signal Process.*, vol. 12, no. 6, pp. 1435–1448, Dec. 2018.
[37] M. Lustig, D. Donoho, and J. M. Pauly, "Sparse MRI: The application of compressed sensing for rapid MR imaging," *Magn. Reson. Med.*, vol. 58, no. 6, pp. 1182–1195, Dec. 2007.
[38] I. Daubechies, M. Defrise, and C. De Mol, "An iterative thresholding algorithm for linear inverse problems with a sparsity constraint," *Commun. Pure Appl. Math.*, vol. 57, no. 11, pp. 1413–1457, Nov. 2004.
[39] P. R. Hill, J.-H. Kim, A. Basarab, D. Kouame, D. R. Bull, and A. Achim, "Compressive imaging using approximate message passing and a cauchy prior in the wavelet domain," in *Proc. IEEE Int. Conf. Image Process. (ICIP)*, Arizona, AZ, USA, Sep. 2016, pp. 2514–2518.
[40] U. S. Kamilov, H. Mansour, and B. Wohlberg, "A Plug-and-Play priors approach for solving nonlinear imaging inverse problems," *IEEE Signal Process. Lett.*, vol. 24, no. 12, pp. 1872–1876, Dec. 2017.
[41] A. Brifman, Y. Romano, and M. Elad, "Turning a denoiser into a super-resolver using plug and play priors," in *Proc. IEEE Int. Conf. Image Process. (ICIP)*, Phoenix, AZ, USA, 2016, pp. 1404–1408.
[42] J. Huang, S. Zhang, and D. Metaxas, "Efficient MR image reconstruction for compressed MR imaging," *Med. Image Anal.*, vol. 15, no. 5, pp. 670–679, Oct. 2011.
[43] T. Huang, W. Dong, X. Xie, G. Shi, and X. Bai, "Mixed noise removal via Laplacian scale mixture modeling and nonlocal low-rank approximation," *IEEE Trans. Image Process.*, vol. 26, no. 7, pp. 3171–3186, Jul. 2017.
[44] R. Liu, Y. Zhang, S. Cheng, X. Fan, and Z. Luo, "A theoretically guaranteed deep optimization framework for robust compressive sensing MRI," in *Proc. AAAI Conf. Artif. Intell.*, New York, NY, USA, 2019, pp. 4368–4375.

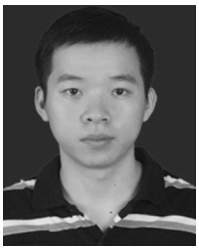

ZHONG-HUA XIE received the Ph.D. degree in information and communication engineering from the South China University of Technology, China, in 2018. He is currently a Lecturer with the School of Computer Science and Engineering, Huizhou, China. His research interests include inverse problems in image processing, deep learning, and medical imaging.

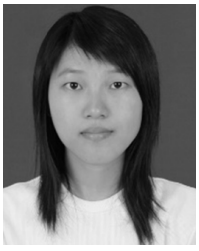

LING-JUN LIU received the Ph.D. degree in information and communication engineering from the South China University of Technology, China, in 2015. From September 2015 to June 2018, she held a Postdoctoral Research position with SCUT. She is currently a Lecturer with the School of Computer Science and Engineering, Huizhou, China. Her research interests include signal processing, intelligent computing, and computerized tomography.

XIAO-YE WANG received the B.S. degree in communication engineering from the Hunan University of Science and Engineering, Hunan, China, in 2010, and the M.S. degree in communication and information system, and the Ph.D. degree in information and communication engineering from Shenzhen University, Shenzhen, China, in 2013 and 2019, respectively. She is currently a Lecturer with the School of Computer Science and Engineering, Huizhou, China. Her current research interests include array signal processing, space-time adaptive processing, and compressive sensing.

CUI YANG was born in September 1983. She received the B.S. and Ph.D. degrees from the South China University of Technology (SCUT), Guangzhou, China, in 2005 and 2010, respectively. She is currently an Associate Professor with the School of Electronic and Information Engineering, SCUT. Her research interests include digital signal processing and communications.